Iterative Per-Vector Equalization for Orthogonal Signal-Division Multiplexing Over Time-Varying Underwater Acoustic Channels

Han, Jing; Chepuri, Sundeep Prabhakar; Zhang, Qunfei; Leus, Geert

Important note
To cite this publication, please use the final published version (if applicable).
Please check the document version above.

Iterative Per-Vector Equalization for Orthogonal Signal-Division Multiplexing Over Time-Varying Underwater Acoustic Channels

Jing Han , *Member, IEEE*, Sundeep Prabhakar Chepuri , *Member, IEEE*, Qunfei Zhang , *Member, IEEE*, and Geert Leus , *Fellow, IEEE*

Abstract—Orthogonal signal-division multiplexing (OSDM) is a promising modulation scheme that provides a generalized framework to unify orthogonal frequency-division multiplexing (OFDM) and single-carrier frequency-domain equalization. By partitioning each data block into vectors, it allows for a flexible configuration to trade off resource management flexibility with peak-to-average power ratio. In this paper, an OSDM system is proposed for underwater acoustic communications. The channel Doppler effect after front-end resampling is modeled as a common time-varying phase on all propagation paths. It leads to a special signal distortion structure in the OSDM system, namely, intervector interference, which is analogous to the intercarrier interference in the conventional OFDM system. To counteract the related performance degradation, the OSDM receiver performs iterative detection, integrating joint channel impulse response and phase estimation, equalization, and decoding in a loop. Meanwhile, to avoid inversion of large matrices in channel equalization, frequency-domain per-vector equalization is designed, which can significantly reduce the computational complexity. Furthermore, the performance of the proposed OSDM system is evaluated through both numerical simulations and a field experiment, and its reliability over underwater acoustic channels is confirmed.

Index Terms—Orthogonal signal-division multiplexing (OSDM), time-varying channels, turbo equalization, underwater acoustic communications.

I. INTRODUCTION

UNDERWATER acoustic (UWA) channels are considered as one of the most challenging communication media in use [1]. Specifically, UWA channels exhibit limited available bandwidth, typically of the order of 10 kHz for medium-range links, due to the frequency-dependent transmission loss. Also, UWA channels suffer from long multipath spread and severe

time variation, usually several orders of magnitude larger than in terrestrial radio channels, due to the low velocity of acoustic waves (nominally 1500 m/s).

To achieve reliable transmission with high bandwidth efficiency over UWA channels, a number of modulation schemes and receiver algorithms have been investigated over the last three decades. Among them, a successful phase-coherent communication with single-carrier modulation (SCM) was demonstrated in [2], where the receiver combines an adaptive time-domain equalizer (TDE) with a phase-locked loop (PLL) to combat time-varying intersymbol interference (ISI). Although this TDE-PLL structure has been accepted thereafter as a standard method and further adopted to several systems [3]–[5], its performance and complexity depend heavily on the choice of receiver parameters, such as the TDE length and the PLL coefficients. This may impair robustness and restrict practical implementations [6]. To cope with these problems, two low-complexity techniques, namely, orthogonal frequency-division multiplexing (OFDM) and single-carrier frequency-domain equalization (SC-FDE), have received much attention in recent years (see [7], [8] and reference therein). Both schemes are based on blockwise frequency-domain processing using discrete Fourier transform (DFT), which allows for mitigating the channel frequency selectivity more efficiently. However, it is well known that OFDM systems suffer from a large peak-to-average power ratio (PAPR) and a high sensitivity to Doppler effects [7]. On the other hand, the SC-FDE system offers lower PAPR and better Doppler tolerance, yet at the expense of an inflexible bandwidth and energy management [9], [10].

As another promising alternative, orthogonal signal-division multiplexing (OSDM) was first proposed in [11] and [12], and recently applied for UWA communications in [13] and [14]. Mathematically, it is worth noting that OSDM shares a similar signal structure with vector OFDM, which was independently developed in [15]. At the transmitter, different from conventional OFDM where the data block is treated as a whole and modulated by a single full-length inverse DFT (IDFT), these schemes split the data block into segments (termed as *vectors* herein) and perform several componentwise IDFTs with length reduced to the number of vectors. By doing so, they attain a unified framework to trade off resource management flexibility with PAPR, thus bridging the gap between OFDM and SC-FDE. As for the receiver design, most existing studies in terrestrial

radio communications usually assume the channel to be time-invariant and known *a priori* [16]–[18], which is not valid for practical underwater scenarios. To this end, the OSDM scheme in [13] utilizes a pilot vector dedicated to channel estimation. Although not taking the channel time variation into account, tank test results show that OSDM outperforms conventional OFDM and SCM with the TDE-PLL receiver. Furthermore, by explicitly accommodating Doppler spreads using a basis expansion model (BEM), the Doppler-resilient OSDM (D-OSDM) scheme in [14] has the capability to achieve a reliable communication over time-varying UWA channels.

However, there are two problems arising in the D-OSDM system. 1) At the transmitter, zero vectors are inserted into each transmitted block to preserve the orthogonality of the pilot and data vectors. This method is an extension of the null-subcarrier insertion scheme for the OFDM system in [19], by which channel estimation and data detection can be separated and thus simplified. Since the required number of zero vectors increases with the maximum Doppler shift [14], this system will suffer a significant loss in bandwidth efficiency. 2) At the receiver, the channel equalization in [14] is performed directly on the demodulated vectors. It requires channel matrix inversion and incurs a complexity of $\mathcal{O}(M^3)$ for each vector, where M denotes the OSDM vector length. However, it is also assumed that M is longer than the channel delay spread to make channel estimation easier. This system will, therefore, be computationally expensive for UWA channels with long delay spread.

The aim of this paper is to address the above-mentioned problems. The main contributions are detailed as follows.

1) To avoid the overhead of zero vectors introduced for the BEM coefficient estimation process, a time-varying phase model is adopted, which has been proven to be valid in multiple systems (see, e.g., [2], [20], [21]). However, it is shown that, unlike the effects of carrier fluctuation in SCM or intercarrier interference (ICI) in OFDM, the time variation in the OSDM system leads to inter-vector interference (IVI). As a result, most of the existing phase estimation and compensation methods cannot be directly applied to OSDM. Therefore, in this paper, we leverage the slowly varying nature of the phase, and characterize it with fewer parameters in both frequency and time domains. Based on that, we further design an alternating least squares (ALS) algorithm to perform joint channel impulse response (CIR) and phase estimation.

2) To alleviate the cubic complexity of channel equalization, the approach proposed in this paper combines soft interference cancellation (SIC) and phase compensation (PC) operations with frequency-domain equalization (FDE). The motivation behind such a design is twofold. First, with the aid of SIC and PC, the channel time variation is mitigated and the demodulated vectors can be decoupled. Channel equalization is thus allowed to be imposed on each vector instead of on the entire block (or on vector groups such as in [14]), by which dimensionality reduction is achieved. Second, by exploiting the channel matrix structure, the per-vector equalization is performed

in the frequency domain on predistorted versions of the demodulated vectors. It avoids inverting the channel matrix directly. Moreover, we provide a multichannel FDE extension for OSDM to collect spatial gains. Quantitatively, the complexity of the proposed FDE algorithms is about $\mathcal{O}(M\log_2 M)$ per vector, which is more tractable for practical applications.

Furthermore, another feature of the proposed OSDM system is that each data vector is encoded independently at the transmitter. By virtue of it, the receiver can be designed to perform per-vector equalization and decoding iteratively based on the turbo principle. We evaluate the performance of the proposed OSDM system through both numerical simulations and a shallow-water field experiment, and its reliability over time-varying UWA channels is confirmed.

The remainder of this paper is organized as follows. In Section II, we present the OSDM signal model and the UWA channel model. In Section III, we describe the iterative OSDM receiver algorithm in detail, based on which further discussions on the receiver structure and complexity are provided in Section IV. The numerical simulations and experimental results are then presented in Sections V and VI, respectively. Finally, conclusions are drawn in Section VII.

Notation: $(\cdot)^*$ stands for conjugate, $(\cdot)^T$ for transpose, and $(\cdot)^H$ for Hermitian transpose. We reserve $|\cdot|$ for the absolute value, $\|\cdot\|$ for the Euclidean norm, and $\otimes$ for the Kronecker product. We use $\mathbf{0}_M$, $\mathbf{1}_M$, $\mathbf{I}_M$, and $\mathbf{e}_M(m)$ to represent the $M \times 1$ all-zero vector, the $M \times 1$ all-one vector, the $M \times M$ identity matrix, and the mth column of $\mathbf{I}_M$, respectively. $\mathbf{F}_N$ denotes the $N \times N$ unitary discrete Fourier transform (DFT) matrix, and $\text{diag}\{\mathbf{x}\}$ denotes a diagonal matrix with $\mathbf{x}$ on its diagonal. Meanwhile, we define $[\mathbf{x}]_n$ as the nth entry of the column vector $\mathbf{x}$, and $[\mathbf{X}]_{m,n}$ as the (m,n)th entry of the matrix $\mathbf{X}$, where all indices are starting from 0. Furthermore, $[\mathbf{x}]_{m:n}$ indicates the subvector of $\mathbf{x}$ from entry m to n, and $[\mathbf{X}]_{m:n,p:q}$ indicates the submatrix of $\mathbf{X}$ from row m to n and from column p to q, where only the colon is kept when all rows or columns are included.

II. SIGNAL MODEL

A. Transmitted Signal

Our OSDM transmission scheme is depicted in the upper part of Fig. 1. We consider a transmission block of $K_a = NM_a$ bits. Instead of being treated as a whole such as in OFDM systems, here the block is further partitioned into bit vectors $\{\mathbf{a}_n\}_{n=0}^{N-1}$ of length M_a, on each of which independent operations including encoding, interleaving, and mapping are performed in parallel. To be specific, the nth bit vector $\mathbf{a}_n$ is encoded using a convolutional encoder to produce a coded vector $\mathbf{b}_n$ of length $M_c = (M_a + M_t)/R_c$, where $R_c \in (0,1]$ is the coding rate and $M_t \geq 0$ is the overhead introduced by the encoder, including a cyclic redundancy check (CRC) code to examine data integrity and a termination sequence to reset the final state of the encoder. The encoded bits are then shuffled by a random interleaver and grouped into M sets of Q bits, i.e., $\mathbf{c}_n = [\mathbf{c}_{n,0}^T, \mathbf{c}_{n,1}^T, \ldots, \mathbf{c}_{n,M-1}^T]^T$, where $M = M_c/Q$
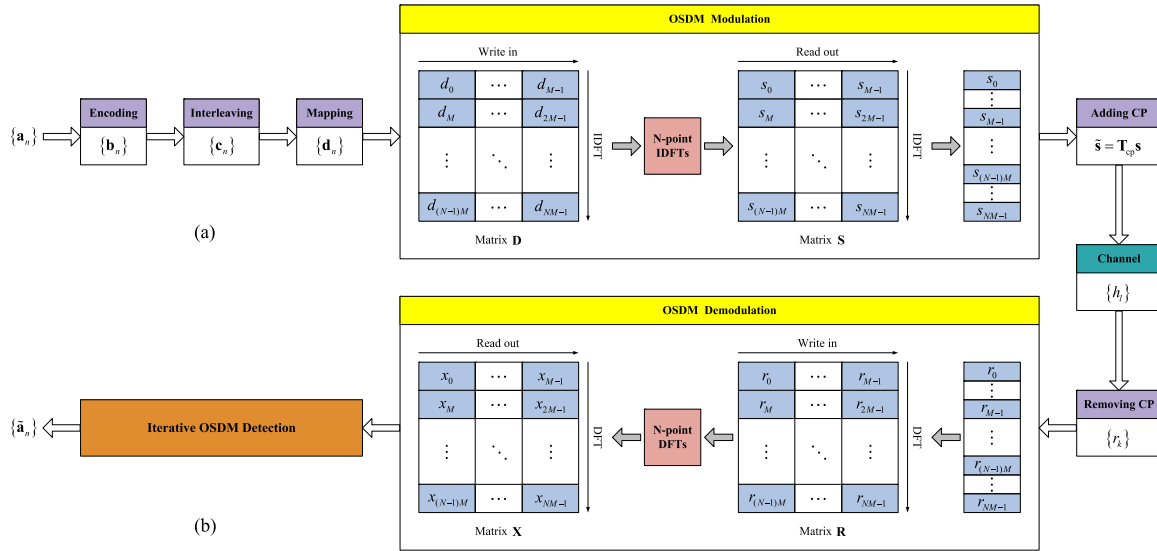
Fig. 1.   Block diagram of the proposed OSDM system. (a) OSDM transmitter structure. (b) OSDM receiver structure.

and $\mathbf{c}_{n,m} = [c_{n,m}(0), c_{n,m}(1), \ldots, c_{n,m}(Q-1)]^T \in \{0,1\}^Q$. Subsequently, each set of Q successive interleaved bits $\mathbf{c}_{n,m}$ is mapped onto a 2^Q-ary complex-valued symbol from a constellation $\mathcal{A} = \{\tilde{\alpha}_1, \tilde{\alpha}_2, \ldots, \tilde{\alpha}_{2^Q}\}$ with $\tilde{\alpha}_i$ corresponding to the bit pattern $\tilde{\mathbf{c}}_i = [\tilde{c}_i(0), \tilde{c}_i(1), \ldots, \tilde{c}_i(Q-1)]^T$. We thus get the nth symbol vector $\mathbf{d}_n = [d_{n,0}, d_{n,1}, \ldots, d_{n,M-1}]^T$, where $d_{n,m} = \tilde{\alpha}_i$ if $\mathbf{c}_{n,m} = \tilde{\mathbf{c}}_i$. Note that due to the unique structure of the OSDM block, we use the two subscripts n and m in this paper to index symbols. Alternatively, to simplify some representations in the following, we also stack $\{\mathbf{d}_n\}$ into a symbol block of length $K = MN$ and use a single indexing, i.e., $\mathbf{d} = [d_0, d_1, \ldots, d_{K-1}]^T$. These two notations can be readily converted into each other with $d_{nM+m} = d_{n,m}$.

Now, the OSDM modulation can be implemented by a three-step procedure. First, the symbols in $\mathbf{d}$ are written rowwise into an $N \times M$ matrix $\mathbf{D}$ with its nth row filled by the nth symbol vector $\mathbf{d}_n^T$. Second, N-point IDFTs are performed columnwise to the matrix $\mathbf{D}$ yielding $\mathbf{S} = \mathbf{F}_N^H \mathbf{D}$. Third, the resulting matrix $\mathbf{S}$ is read out rowwise to obtain the baseband transmitted signal $\mathbf{s} = [s_0, s_1, \ldots, s_{K-1}]^T$. It can be seen that unlike conventional OFDM which modulates the symbols in $\mathbf{d}$ one-to-one on K subcarriers and generates time-domain samples using a K-point IDFT, OSDM divides $\mathbf{d}$ into N symbol vectors $\{\mathbf{d}_n\}$ of length M and produces the baseband signal by componentwise N-point IDFTs. Therefore, in comparison with OFDM, OSDM possesses a lower PAPR due to the reduction in the IDFT size (by a factor of M), while potentially offering frequency diversity within each vector.

To formulate the OSDM modulation mathematically, we define the $K \times K$ permutation matrix

$$\mathbf{P}_{N,M} = \begin{bmatrix} \mathbf{I}_N \otimes \mathbf{e}_M^T(0) \\ \mathbf{I}_N \otimes \mathbf{e}_M^T(1) \\ \vdots \\ \mathbf{I}_N \otimes \mathbf{e}_M^T(M-1) \end{bmatrix}. \tag{1}$$

The above modulation process can then be expressed as

$$\mathbf{s} = \mathbf{P}_{N,M}^H \left(\mathbf{I}_M \otimes \mathbf{F}_N^H \right) \mathbf{P}_{N,M} \mathbf{d}$$
$$= \left(\mathbf{F}_N^H \otimes \mathbf{I}_M \right) \mathbf{d} \tag{2}$$

where, in the first equation, matrices $\mathbf{P}_{N,M}$, $\mathbf{I}_M \otimes \mathbf{F}_N^H$ and $\mathbf{P}_{N,M}^H$ correspond to the rowwise write, N-point IDFT and rowwise read operations, respectively.

Note that, similar to [13] and [14], it is assumed in this paper that $M > L$, where L is the maximum memory length of the discrete-time CIR. As a result, we can just reserve the first symbol vector $\mathbf{d}_0$ as the pilot vector to facilitate the initial channel estimation at the receiver side. Moreover, a cyclic prefix (CP) of length $K_g > L$ is added at the beginning of each block to eliminate interblock interference (IBI), i.e., $\tilde{\mathbf{s}} = \mathbf{T}_{cp}\mathbf{s}$, where $\mathbf{T}_{cp} = [\mathbf{I}_{cp}, \mathbf{I}_K]^T$ with $\mathbf{I}_{cp}$ comprising the last K_g columns of $\mathbf{I}_K$. Finally, the sequence $\tilde{\mathbf{s}}$ is upconverted to the carrier frequency f_c and then transmitted through a UWA channel.

B. Channel Model and Received Signal

It is known that under the UWA channel assumption that path amplitudes are constant during one block and a common Doppler scale is shared among all paths, the effect of time variation in wideband signals approximately reduces to a carrier frequency offset (CFO) after Doppler compensation at the receiver via resampling [20]. Accordingly, the baseband received signal after CP removal can be expressed as

$$r_k = \sum_{l=0}^{L} h_l e^{j\theta_k} s_{k-l} + n_k, \quad k = 0, \ldots, K-1 \tag{3}$$

where n_k is the additive noise term, h_l is the CIR, and $\theta_k = 2\pi\epsilon k T_s$ stands for the phase corresponding to the postre-sampling CFO ϵ with T_s being the sampling period. Moreover, the index of s in (3) is actually taken modulo-K due to the circular convolution implemented by the CP.

In this paper, we further eliminate the single-frequency restriction imposed on the time-varying phase, and consider $\{\theta_k\}_{k=0}^{K-1}$ as a deterministic sequence with slow variation to accommodate other effects of channel time variation that cannot be aggregated into a common Doppler scale, such as drifting of the platforms, scattering in the medium and slight Doppler spread among different paths, etc. Note that a similar channel model is also adopted for single-carrier UWA communications, where a symbolwise PLL [2] and a groupwise correction [21] have been employed for tracking θ_k. However, these methods are not applicable to blockwise modulations such as OSDM. To estimate and compensate θ_k in this case, we first establish the model of the received signal distorted by the time-varying phase below.

As shown in the lower part of Fig. 1, the OSDM demodulation is based on componentwise N-point DFTs, which reverses the modulation process at the transmitter. Here, we also adopt the previously mentioned single indexing and define the received signal block as $\mathbf{r} = [r_0, r_1, \ldots, r_{K-1}]^T$. Specifically, the interleaver first writes the samples of $\mathbf{r}$ rowwise into an $N \times M$ matrix $\mathbf{R}$. Then, N-point DFTs are performed columnwise to the matrix $\mathbf{R}$ yielding $\mathbf{X} = \mathbf{F}_N \mathbf{R}$. Finally, the matrix $\mathbf{X}$ is read out rowwise to obtain the demodulated block $\mathbf{x} = [x_0, x_1, \ldots, x_{K-1}]^T$. Analogous to (2), the OSDM demodulation process can be expressed as

$$\mathbf{x} = \mathbf{P}_{N,M}^H \left(\mathbf{I}_M \otimes \mathbf{F}_N \right) \mathbf{P}_{N,M} \mathbf{r}$$
$$= \left(\mathbf{F}_N \otimes \mathbf{I}_M \right) \mathbf{r}. \tag{4}$$

Now, from (2)–(4), the input–output relationship of the time-varying OSDM system can be written in the matrix-vector form as

$$\mathbf{x} = \left(\mathbf{F}_N \otimes \mathbf{I}_M \right) \tilde{\boldsymbol{\Theta}} \tilde{\mathbf{H}} \left(\mathbf{F}_N^H \otimes \mathbf{I}_M \right) \mathbf{d} + \mathbf{z} \tag{5}$$

where $\tilde{\mathbf{H}}$ is the $K \times K$ circulant channel matrix with first column equal to the CIR vector $\mathbf{h} = [h_0, h_1, \ldots h_L]^T$ appended by $K - L - 1$ zeros, $\tilde{\boldsymbol{\Theta}} = \mathrm{diag}\{[e^{j\theta_0}, e^{j\theta_1}, \ldots, e^{j\theta_{K-1}}]\}$ is the time-varying phase matrix, and $\mathbf{z} = [z_0, z_1, \ldots, z_{K-1}]^T$ is the noise term. To separate the time-varying and time-invariant channel effects, we reformulate the signal model (5) into

$$\mathbf{x} = \mathbf{GHd} + \mathbf{z}. \tag{6}$$

It can be derived that

$$\mathbf{H} = \left(\mathbf{F}_N \otimes \mathbf{I}_M \right) \tilde{\mathbf{H}} \left(\mathbf{F}_N^H \otimes \mathbf{I}_M \right)$$
$$= \begin{bmatrix} \mathbf{H}_0 & & & \\ & \mathbf{H}_1 & & \\ & & \ddots & \\ & & & \mathbf{H}_{N-1} \end{bmatrix} \tag{7}$$

where $\mathbf{H}_n, n = 0, \ldots, N-1$, is the $M \times M$ channel submatrix corresponding to the nth symbol vector, which has the form

$$\mathbf{H}_n = \boldsymbol{\Lambda}_M^{nH} \mathbf{F}_M^H \bar{\mathbf{H}}_n \mathbf{F}_M \boldsymbol{\Lambda}_M^n \tag{8}$$

with $\boldsymbol{\Lambda}_M^n = \mathrm{diag}\{[1, e^{-j\frac{2\pi n}{K}}, \ldots, e^{-j\frac{2\pi n}{K}(M-1)}]\}$ referred to as the frequency shifting submatrix, and $\bar{\mathbf{H}}_n = \mathrm{diag}$

$\{[H_n, H_{N+n}, \ldots, H_{(M-1)N+n}]\}$ as the decimated frequency response (DFR) submatrix, since $H_k = \sum_{l=0}^{L} h_l e^{-j(2\pi/K)lk}$ for $k = 0, \ldots, K-1$. Meanwhile, it can also be shown in (6) that

$$\mathbf{G} = \left(\mathbf{F}_N \otimes \mathbf{I}_M \right) \tilde{\boldsymbol{\Theta}} \left(\mathbf{F}_N^H \otimes \mathbf{I}_M \right)$$
$$= \begin{bmatrix} \mathbf{G}_0 & \mathbf{G}_{N-1} & \ldots & \mathbf{G}_1 \\ \mathbf{G}_1 & \mathbf{G}_0 & \ldots & \mathbf{G}_2 \\ \vdots & \vdots & \ddots & \vdots \\ \mathbf{G}_{N-1} & \mathbf{G}_{N-2} & \ldots & \mathbf{G}_0 \end{bmatrix} \tag{9}$$

where $\mathbf{G}_i$, $i = 0, \ldots, N-1$, is the phase submatrix corresponding to the ith frequency sample, which has the form

$$\mathbf{G}_i = \mathrm{diag}\{\mathbf{g}_i\} \tag{10}$$

with $\mathbf{g}_i = [g_{i,0}, g_{i,1}, \ldots, g_{i,M-1}]^T$ and its entries $g_{i,m} = \frac{1}{N} \sum_{n=0}^{N-1} e^{j(\theta_{nM+m} - 2\pi ni/N)}$ for $m = 0, \ldots, M-1$. It is easy to verify that $\mathbf{G}_{N-i} = \mathbf{G}_{-i}$. The proof of (7)–(10) can be found in Appendix A.

After demodulation, the length-K blocks $\mathbf{x}$ and $\mathbf{z}$ in (6) are divided into N vectors, i.e., $\mathbf{x}_n = [\mathbf{x}]_{nM:nM+M-1}$ and $\mathbf{z}_n = [\mathbf{z}]_{nM:nM+M-1}$ for $n = 0, \ldots, N-1$. It can be seen from (7) and (9) that for time-invariant channels where $\theta_k = 0$ for all k, we have $\mathbf{G} = \mathbf{I}_K$, and thus the detection of the N symbol vectors in the OSDM system can be decoupled as

$$\mathbf{x}_n = \mathbf{H}_n \mathbf{d}_n + \mathbf{z}_n, \qquad n = 0, \ldots, N-1. \tag{11}$$

For this case, maximum likelihood (ML) and linear receivers have already been proposed in the literature (see [18] and references therein). However, for the time-varying case where $\mathbf{G}$ is not diagonal, interference among symbol vectors may arise accordingly, i.e.,

$$\mathbf{x}_n = \mathbf{G}_0 \mathbf{H}_n \mathbf{d}_n + \sum_{i \neq 0} \mathbf{G}_i \mathbf{H}_{n-i} \mathbf{d}_{n-i} + \mathbf{z}_n,$$
$$n = 0, \ldots, N-1. \tag{12}$$

Note that all indices in (12) are taken modulo-N for notational simplicity. It can be seen that on the right-hand side of (12), the first term models the ISI within one vector, the second term represents the IVI, and $\{\mathbf{G}_i\}$ capture the phase distortion due to the channel time variation. In [22], it is assumed that the channel frequency response is *a priori* known or quasi-static over consecutive blocks to compensate phase noise. This assumption is usually inappropriate for rapidly time-varying UWA channels where channel estimation is required on a block-by-block basis. Therefore, we propose an iterative algorithm for OSDM detection in this paper, which will be described in Section III.

III. ITERATIVE OSDM DETECTION

The structure of the iterative OSDM detection is illustrated in Fig. 2, which consists of the following two processing modes.

1) Pilot-based interference-ignored preprocessing mode: This mode is activated at the iteration $\beta = 0$, where initial channel estimation and equalization are performed without explicit IVI cancellation. The resulting CIR and
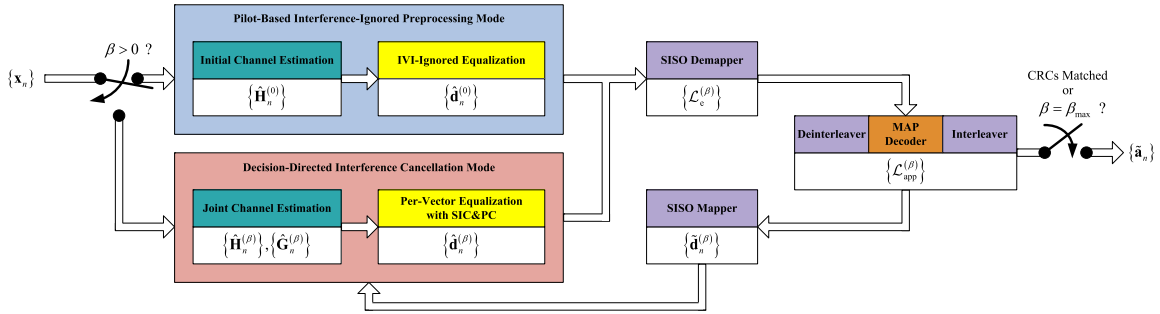
Fig. 2. Structure of the iterative OSDM detection.

symbol estimates are provided as initial values for the following iterations.

2) Decision-directed interference cancellation mode: The receiver switches to this mode for the iterations $\beta > 0$, where the time-varying UWA channel is reconstructed via joint CIR and phase estimation, and then low-complexity per-vector equalization with SIC and PC is performed in the frequency domain to mitigate IVI and ISI. Furthermore, the turbo principle is applied based on the exchange of soft information with the decoder to improve the OSDM system performance iteratively.

The above algorithm continues until the CRCs of all detected symbol vectors are matched successfully, or a prespecified number of iterations $\beta_{\max}$ have elapsed. We next present the detailed descriptions of several key modules.

A. Interference-Ignored Preprocessing

At the initial iteration $\beta = 0$, the residual Doppler effect after front-end resampling is ignored. We, thus, adopt an estimate of $\mathbf{g}_i$ corresponding to the zero-valued phase, i.e.,

$$\hat{\mathbf{g}}_i^{(0)} = \delta_i \mathbf{1}_M \tag{13}$$

where δ_i is the Kronecker delta. As a result, the demodulated signal vector is now reduced to (11), where $\mathbf{z}_n$ contains the noise plus residual inter- and intravector interferences.

We further assume a moderate signal-to-interference-plus-noise ratio in this case, and define an $M \times M$ diagonal frequency-domain symbol matrix $\mathbf{D}_n = \mathrm{diag}\{\mathbf{F}_M \boldsymbol{\Lambda}_M^n \mathbf{d}_n\}$ and an $M \times (L+1)$ matrix $\boldsymbol{\Gamma}_n$ with entries $[\boldsymbol{\Gamma}_n]_{m,l} = e^{-j(2\pi/K)(mN+n)l}$. Since only the pilot vector $\mathbf{d}_0$ is available at this point, based on (11) and the assumption $M > L$, the initial CIR estimate $\hat{\mathbf{h}}^{(0)} = [\hat{h}_0^{(0)}, \hat{h}_1^{(0)}, \ldots \hat{h}_L^{(0)}]^T$ can be obtained in the least squares (LS) sense as

$$\hat{\mathbf{h}}^{(0)} = \frac{1}{M} \boldsymbol{\Gamma}_0^H \mathbf{D}_0^{-1} \mathbf{F}_M \mathbf{x}_0. \tag{14}$$

Therefore, we have the corresponding estimates of the nth DFR and channel submatrices

$$\hat{\bar{\mathbf{H}}}_n^{(0)} = \mathrm{diag}\left\{ \boldsymbol{\Gamma}_n \hat{\mathbf{h}}^{(0)} \right\} \tag{15}$$

$$\hat{\mathbf{H}}_n^{(0)} = \boldsymbol{\Lambda}_M^{nH} \mathbf{F}_M^H \hat{\bar{\mathbf{H}}}_n^{(0)} \mathbf{F}_M \boldsymbol{\Lambda}_M^n \tag{16}$$

and then arrive at the initial symbol estimates

$$\hat{\mathbf{d}}_n^{(0)} = \left(\hat{\mathbf{H}}_n^{(0)} \right)^{-1} \mathbf{x}_n, \qquad n = 1, \ldots, N-1. \tag{17}$$

B. Joint CIR and Phase Estimation

For iterations $\beta > 0$, the residual Doppler effect after front-end resampling is taken into account by modeling it as a time-varying phase and assuming it changes slowly within one block, which is often the case for UWA channels with fixed or smoothly moving transceivers. Moreover, for the OSDM signal model in (12), this time-varying phase can be further simplified as follows.

1) In the frequency domain: It is reasonable to assume that the Doppler spread of the time-varying phase is bounded. We can thus reduce the number of phase submatrices in the model, i.e.,

$$\mathbf{G}_i = \mathbf{0}_{M \times M}, \qquad I < i < N - I \tag{18}$$

where I is the Doppler span parameter.

2) In the time domain: A subvector-fading model can be assumed, i.e., the time-varying phase is approximately constant over $J = M/\bar{M}$ symbols, where $\bar{M}$ and J are integers denoting the number and length of the quasi-static subvectors, respectively. As such, we can reformulate the phase submatrix in (10) as

$$\mathbf{G}_i = \mathrm{diag}\{\mathbf{g}_i\} \otimes \mathbf{I}_J, \qquad -I \leq i \leq I \tag{19}$$

where $\mathbf{g}_i = [g_{i,0}, g_{i,1}, \ldots, g_{i,\bar{M}-1}]^T$.

Under the above assumptions, the demodulated signal vector in (12) can be rewritten in the form

$$\mathbf{x}_n = \sum_{i=-I}^{I} \mathbf{G}_i \mathbf{H}_{n-i} \mathbf{d}_{n-i} + \mathbf{z}_n \tag{20}$$

which, unlike the signal model used in the initial iteration, incorporates the time-varying channel effects explicitly.

1) Iterative Estimation: The CIR and phase can now be jointly estimated by solving

$$\min_{\mathbf{h}, \{\mathbf{g}_i\}} \sum_{n=0}^{N-1} \left\| \mathbf{x}_n - \sum_{i=-I}^{I} \mathbf{G}_i \mathbf{H}_{n-i} \mathbf{d}_{n-i} \right\|^2. \tag{21}$$

However, two issues should be observed here. First, there exists a scaling ambiguity between the estimates of $\mathbf{h}$ and $\{\mathbf{g}_i\}$.
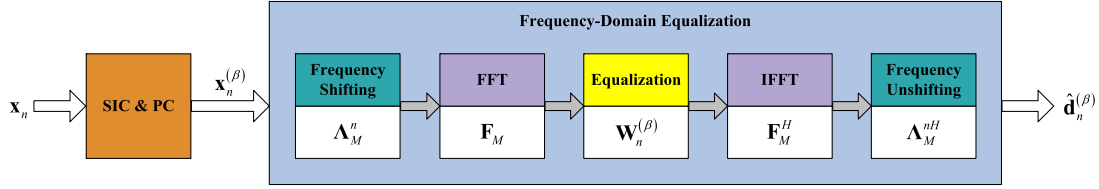
Fig. 3.   Structure of the per-vector equalization scheme.

Second, the optimization problem given by (21) is actually bilinear and thus nonconvex. To avoid the ambiguity and find a suboptimal solution, we design an ALS algorithm in this paper, which decouples the joint estimation into two LS problems and updates the estimates of $\mathbf{h}$ and $\{\mathbf{g}_i\}$ in an iterative way. The details of the ALS algorithm are presented in Appendix B.

2) Initialization and Termination: Since the receiver is switched to the decision-directed interference cancellation mode after the initial turbo iteration $\beta = 0$, we define the input symbol vectors at the βth iteration as

$$\mathbf{d}_n^{(\beta)} = \begin{cases} \mathbf{d}_n, & n = 0 \text{ or } n \in \mathcal{N}_{\mathrm{v}}^{(\beta)} \\ \tilde{\mathbf{d}}_n^{(\beta)}, & n \in \mathcal{N}_{\mathrm{r}}^{(\beta)} \end{cases} \qquad (22)$$

where $\mathcal{N}_{\mathrm{v}}^{(\beta)}$ and $\mathcal{N}_{\mathrm{r}}^{(\beta)}$ are the index sets of the successfully decoded and the remaining symbol vectors up to the βth iteration, respectively, satisfying $\mathcal{N}_{\mathrm{v}}^{(\beta)} \cup \mathcal{N}_{\mathrm{r}}^{(\beta)} = \{1, 2, \ldots, N - 1\}$, and $\{\tilde{\mathbf{d}}_n^{(\beta)}\}$ are the soft symbol vectors fed back from the decoder (see Section III-D for more information).

To solve the optimization problem in (21), we use the decisions $\{\mathbf{d}_n^{(\beta)}\}$ instead of the true symbol vectors. The initial values of the ALS algorithm are set as the CIR estimate $\hat{\mathbf{h}}^{(0)}$ and the phase estimates $\{\hat{\mathbf{g}}_i^{(0)}\}$. If the channel time variation is not severe, we can expect the solution of (21) to be in a neighborhood of $\hat{\mathbf{h}}^{(0)}$ and $\{\hat{\mathbf{g}}_i^{(0)}\}$, and the ALS algorithm can attain it in a moderate number of steps. Therefore, when the ALS algorithm is terminated, the final channel estimates $\hat{\mathbf{h}}^{(\beta)}$ and $\{\hat{\mathbf{g}}_i^{(\beta)}\}$ for the βth iteration are generated. Then, similar to (15) and (16), the estimates of the DFR and channel submatrices can be updated as

$$\hat{\bar{\mathbf{H}}}_{\mathbf{n}}^{(\beta)} = \text{diag}\left\{\mathbf{\Gamma}_n \hat{\mathbf{h}}^{(\beta)}\right\}$$

$$= \text{diag}\left\{\left[\hat{H}_n^{(\beta)}, \hat{H}_{N+n}^{(\beta)}, \ldots, \hat{H}_{(M-1)N+n}^{(\beta)}\right]\right\} \qquad (23)$$

$$\hat{\mathbf{H}}_n^{(\beta)} = \mathbf{\Lambda}_M^{nH} \mathbf{F}_M^H \hat{\bar{\mathbf{H}}}_n^{(\beta)} \mathbf{F}_M \mathbf{\Lambda}_M^n, \quad n = 0, \ldots, N - 1 \qquad (24)$$

while the estimates of the phase submatrices are

$$\hat{\mathbf{G}}_i^{(\beta)} = \text{diag}\left\{\hat{\mathbf{g}}_i^{(\beta)}\right\} \otimes \mathbf{I}_J, \quad i = -I, \ldots, I. \qquad (25)$$

C. Per-Vector Equalization

To achieve reliable OSDM transmission in the presence of ISI and IVI [cf., (20)], we present a per-vector equalization scheme, whose structure is depicted in Fig. 3. Here, the preceding SIC and PC modules are utilized to mitigate IVI and phase distortion, and then low-complexity frequency-domain

equalization processing follows to combat the ISI caused by the symbols within the same vector. More details of this scheme are explained in the following.

1) Soft Interference Cancellation and Phase Compensation: At the βth iteration, given the soft decisions $\{\mathbf{d}_n^{(\beta)}\}$ in (22), as well as the estimates of the channel and phase submatrices $\{\hat{\mathbf{H}}_n^{(\beta)}\}$ and $\{\hat{\mathbf{G}}_i^{(\beta)}\}$ in (24) and (25), the phase distortion and IVI can be explicitly reconstructed and removed from the nth signal vector, which yields

$$\mathbf{x}_n^{(\beta)} = \left(\hat{\mathbf{G}}_0^{(\beta)}\right)^{-1} \left(\mathbf{x}_n - \sum_{0 < |i| \leq I} \hat{\mathbf{G}}_i^{(\beta)} \hat{\mathbf{H}}_{n-i}^{(\beta)} \mathbf{d}_{n-i}^{(\beta)}\right)$$

$$= \mathbf{H}_n \mathbf{d}_n + \mathbf{z}_n^{(\beta)}. \qquad (26)$$

Here, $\mathbf{x}_n^{(\beta)}$ is the Doppler-compensated signal vector which is subsequently used as input for the equalizer. $\mathbf{z}_n^{(\beta)}$ contains the additive noise and residual interference.

2) Frequency-Domain Equalization: Both the zero-forcing (ZF) and minimum mean-square error (MMSE) criteria can be employed to equalize $\mathbf{x}_n^{(\beta)}$ in (26). Since they have a similar structure, we here focus only on the linear ZF equalizer for simplicity, and the performance evaluations of the MMSE equalizer are provided in Section V.

Mathematically, the linear ZF equalization of the OSDM system is equivalent to

$$\hat{\mathbf{d}}_n^{(\beta)} = \left(\hat{\mathbf{H}}_n^{(\beta)}\right)^{-1} \mathbf{x}_n^{(\beta)} \qquad (27)$$

where $\hat{\mathbf{d}}_n^{(\beta)}$ is the estimate of the nth symbol vector. Furthermore, we notice from (24) that

$$\left(\hat{\mathbf{H}}_n^{(\beta)}\right)^{-1} = \mathbf{\Lambda}_M^{nH} \mathbf{F}_M^H \left(\hat{\bar{\mathbf{H}}}_n^{(\beta)}\right)^{-1} \mathbf{F}_M \mathbf{\Lambda}_M^n. \qquad (28)$$

This means that, instead of computing the inverse of $\hat{\mathbf{H}}_n^{(\beta)}$ directly as in [13] and [14], which has a high complexity of $\mathcal{O}(M^3)$, it is favorable to exploit the matrix structure and perform equalization in the frequency domain. To this end, we define $\mathbf{W}_n^{(\beta)} = (\hat{\bar{\mathbf{H}}}_n^{(\beta)})^{-1}$ as the coefficient matrix of the frequency-domain equalizer with

$$\left[\mathbf{W}_n^{(\beta)}\right]_{m,m} = \frac{1}{\hat{H}_{mN+n}^{(\beta)}}, \quad m = 0, \ldots, M - 1 \qquad (29)$$

by which the ZF equalization in (27) can be rewritten as

$$\hat{\mathbf{d}}_n^{(\beta)} = \mathbf{\Lambda}_M^{nH} \mathbf{F}_M^H \mathbf{W}_n^{(\beta)} \mathbf{F}_M \mathbf{\Lambda}_M^n \mathbf{x}_n^{(\beta)}. \qquad (30)$$

Moreover, recall that $(\hat{\mathbf{H}}_n^{(0)})^{-1}$ in (17) can be factorized similarly as (28); therefore, frequency-domain equalization is actually also utilized in the preprocessing step for initial symbol vector estimation.

3) Multichannel Combining: It is well known that multichannel combining at the receiver collects spatial diversity gains and thus has better resilience against deep channel fading [23], [24]. We now consider an OSDM system with P receive elements. In this case, the previous CIR and phase estimation step is performed elementwise, while equalization and multichannel combining are carried out on a vector-by-vector basis. We define $\mathbf{H}_{p,n}$, $\mathbf{x}_{p,n}^{(\beta)}$, and $\mathbf{z}_{p,n}^{(\beta)}$ as the nth channel submatrix, Doppler-compensated signal vector, and noise vector at the pth receive element, respectively. By stacking the signal vectors of all P channels together, i.e.,

$$
\begin{bmatrix} \mathbf{x}_{1,n}^{(\beta)} \\ \vdots \\ \mathbf{x}_{P,n}^{(\beta)} \end{bmatrix} = \begin{bmatrix} \mathbf{H}_{1,n} \\ \vdots \\ \mathbf{H}_{P,n} \end{bmatrix} \mathbf{d}_n + \begin{bmatrix} \mathbf{z}_{1,n}^{(\beta)} \\ \vdots \\ \mathbf{z}_{P,n}^{(\beta)} \end{bmatrix}
\tag{31}
$$

the estimate of the nth symbol vector obtained by multichannel combining can be expressed as

$$
\hat{\mathbf{d}}_n^{(\beta)} = \left(\begin{bmatrix} \hat{\mathbf{H}}_{1,n}^{(\beta)} \\ \vdots \\ \hat{\mathbf{H}}_{P,n}^{(\beta)} \end{bmatrix}^H \begin{bmatrix} \hat{\mathbf{H}}_{1,n}^{(\beta)} \\ \vdots \\ \hat{\mathbf{H}}_{P,n}^{(\beta)} \end{bmatrix} \right)^{-1} \begin{bmatrix} \hat{\mathbf{H}}_{1,n}^{(\beta)} \\ \vdots \\ \hat{\mathbf{H}}_{P,n}^{(\beta)} \end{bmatrix}^H \begin{bmatrix} \mathbf{x}_{1,n}^{(\beta)} \\ \vdots \\ \mathbf{x}_{P,n}^{(\beta)} \end{bmatrix}
\tag{32}
$$

Likewise, let us define the estimate of the channel frequency response corresponding to the pth element at the βth iteration as $\{\hat{H}_{p,k}^{(\beta)}\}_{k=0}^{K-1}$. We can then readily obtain the diagonal coefficient matrix $\mathbf{W}_{p,n}^{(\beta)}$, whose (m,m)th entry has the form

$$
\left[\mathbf{W}_{p,n}^{(\beta)} \right]_{m,m} = \frac{\hat{H}_{p,mN+n}^{(\beta)*}}{\sum_{i=1}^{P} \left| \hat{H}_{i,mN+n}^{(\beta)} \right|^2}, \quad m = 0, \dots, M-1
\tag{33}
$$

and the multichannel combining in (32) can be alternatively performed in the frequency domain as

$$
\hat{\mathbf{d}}_n^{(\beta)} = \sum_{p=1}^{P} \boldsymbol{\Lambda}_M^{nH} \mathbf{F}_M^H \mathbf{W}_{p,n}^{(\beta)} \mathbf{F}_M \boldsymbol{\Lambda}_M^n \mathbf{x}_{p,n}^{(\beta)}.
\tag{34}
$$

D. Decoding

After channel estimation and equalization, the resulting estimates $\hat{\mathbf{d}}_n^{(\beta)} = [\hat{d}_{n,0}^{(\beta)}, \hat{d}_{n,1}^{(\beta)}, \dots, \hat{d}_{n,M-1}^{(\beta)}]^T$ are utilized to update the soft information for each symbol vector $n \in \mathcal{N}_r^{(\beta)}$. As shown in Fig. 2, a soft-input soft-output (SISO) demapper is first employed to compute the extrinsic log-likelihood ratios (LLRs) of the interleaved bits. Here, we adopt the typical assumption that $\hat{d}_{n,m}^{(\beta)} = \mu_n^{(\beta)} d_{n,m} + \xi_n^{(\beta)}$ with $\xi_n^{(\beta)}$ Gaussian distributed with zero mean and variance $\sigma_n^{2(\beta)}$. The extrinsic LLR of the qth bit in $\mathbf{c}_{n,m}$, i.e., $c_{n,m}(q)$, can thus be expressed as (35) shown at the bottom of the page, where $q = 0, \dots, Q-1$, and $\mathcal{L}^{(\beta)}(c_{n,m}(q))$ is the *a priori* LLR at the βth iteration [25]. Moreover, the parameters $\mu_n^{(\beta)}$ and $\sigma_n^{2(\beta)}$ are computed by [26], [27]

$$
\mu_n^{(\beta)} = \frac{1}{M} \sum_{m=0}^{M-1} \frac{\hat{d}_{n,m}^{(\beta)}}{\check{d}_{n,m}^{(\beta)}}
\tag{36}
$$

$$
\sigma_n^{2(\beta)} = \frac{1}{M-1} \sum_{m=0}^{M-1} \left| \hat{d}_{n,m}^{(\beta)} - \mu_n^{(\beta)} \check{d}_{n,m}^{(\beta)} \right|^2
\tag{37}
$$

where $\check{d}_{n,m}^{(\beta)} = \text{dec}\{\hat{d}_{n,m}^{(\beta)}\}$ is the hard symbol decision.

The extrinsic LLRs $\{\mathcal{L}_e^{(\beta)}(c_{n,m}(q))\}$ are then input to a decoder implemented by the standard BCJR algorithm [28], which, in conjunction with a pair of random interleaver and deinterleaver, produces the *a posteriori* LLRs $\{\mathcal{L}_{app}^{(\beta)}(c_{n,m}(q))\}$. Afterwards, based on a CRC, the successfully decoded symbol vectors are reassigned to $\mathcal{N}_v^{(\beta+1)}$, and the remaining symbol vectors update their *a priori* LLRs as $\mathcal{L}^{(\beta+1)}(c_{n,m}(q)) = \mathcal{L}_{app}^{(\beta)}(c_{n,m}(q))$. Furthermore, the soft information $\tilde{\mathbf{d}}_n^{(\beta+1)} = [\tilde{d}_{n,0}^{(\beta+1)}, \tilde{d}_{n,1}^{(\beta+1)}, \dots, \tilde{d}_{n,M-1}^{(\beta+1)}]^T$, $n \in \mathcal{N}_r^{(\beta+1)}$, is computed by a SISO mapper, i.e.,

$$
\tilde{d}_{n,m}^{(\beta+1)} = \sum_{i=1}^{2^Q} \left(\tilde{\alpha}_i \prod_{q=0}^{Q-1} \frac{1}{2} \left(1 + (1 - 2\tilde{c}_i(q)) \right. \right.
$$
$$
\left. \left. \times \tanh\left(\frac{\mathcal{L}_{app}^{(\beta)}(c_{n,m}(q))}{2} \right) \right) \right)
\tag{38}
$$

and fed back for the next iteration [25]. Finally, the decoder releases bit vector decisions $\{\tilde{\mathbf{a}}_n\}_{n=0}^{N-1}$ when the turbo iteration ends.

Remark: In the OSDM detection scheme described above, although per-vector equalization is used in (30) and (34), the decoding is performed in a batch manner, i.e., no soft decisions are updated until all symbol vector estimates are obtained. For this reason, we refer to the scheme as parallel iterative detection (PID). In comparison, since encoding at the transmitter is conducted independently for each symbol vector, the decoding can also be performed on a vector-by-vector basis, i.e., once one symbol vector estimate is obtained, its soft decision is immediately computed and fed back to update channel estimates and improve IVI cancellation for the next symbol vector. We term this latter scheme as successive iterative detection (SID), which can be expected to have better performance than PID.

$$
\mathcal{L}_e^{(\beta)}(c_{n,m}(q)) = \ln \frac{\sum_{\forall \tilde{\mathbf{c}}_i : \tilde{c}_i(q) = 0} \exp \left(-\frac{\left| \hat{d}_{n,m}^{(\beta)} - \mu_n^{(\beta)} \tilde{\alpha}_i \right|^2}{\sigma_n^{2(\beta)}} + \sum_{\forall q' : q' \neq q} \frac{1 - 2\tilde{c}_i(q')}{2} \mathcal{L}^{(\beta)}(c_{n,m}(q')) \right)}{\sum_{\forall \tilde{\mathbf{c}}_i : \tilde{c}_i(q) = 1} \exp \left(-\frac{\left| \hat{d}_{n,m}^{(\beta)} - \mu_n^{(\beta)} \tilde{\alpha}_i \right|^2}{\sigma_n^{2(\beta)}} + \sum_{\forall q' : q' \neq q} \frac{1 - 2\tilde{c}_i(q')}{2} \mathcal{L}^{(\beta)}(c_{n,m}(q')) \right)}
\tag{35}
$$

Source			Complexity
Pilot-based interference-ignored preprocessing mode ($\beta = 0$)	Channel estimation		$\frac{NM+3}{2}\log_2 M + M + (L+1)N$
	Channel equalization (per vector)		$M\log_2 M + 3M$
Decision-directed interference cancellation mode ($\beta > 0$)	Channel estimation (per update)	$\mathbf{h}$ & $\{\bar{\mathbf{H}}_n\}$	$\frac{3}{2}NM\log_2 M + (2I+3)NM + 2(L+1)N$
		$\{\mathbf{G}_i\}$	$\frac{1}{2}NM\log_2 M + (\bar{I}^2 + \bar{I} + 2)NM + \Sigma_{\bar{I}}\bar{M}$
	Channel equalization (per vector)		$\bar{I}M\log_2 M + 4\bar{I}M$

IV. FURTHER DISCUSSIONS

A. Comparisons With Other Existing Systems

1) Signal Structure: It can be seen from (2) that the transmitted signal of OSDM reduces to that of the conventional OFDM and SC-FDE when $N = K$ and $N = 1$, respectively. Otherwise, it consists of N superimposed symbol vectors of length M. The OSDM modulation may also look similar to the modulation scheme whose transmitted signal consists of M CP-free OFDM blocks of length N, i.e., $\mathbf{s}' = (\mathbf{I}_M \otimes \mathbf{F}_N^H)\mathbf{d}$. However, the channel equalization in the latter case will be much more complicated than the per-vector equalization proposed here for OSDM, since IBI will arise therein without CPs. In addition, compared with the OSDM system in [14], the proposed scheme here requires no insertion of zero vectors and performs encoding on a vector-by-vector basis. As such, higher bandwidth efficiency and iterative per-vector equalization can be achieved. Furthermore, the parallel transmission property of the OSDM may be reminiscent of the multiband scheme discussed in [26] and [29]; however, their signal structures are fundamentally different. To be specific, the multiband scheme modulates a common symbol stream onto N separated subbands, while the OSDM scheme allocates distinct symbol vectors onto N interleaved subbands represented by $\{\mathbf{H}_n\}$ in (8). Another widely used parallel transmission scheme is MIMO-OFDM (see [30] for an example). However, unlike the MIMO-OFDM system performing per-subcarrier equalization based on $P_r \times P_t$ channel matrices [30, (4)], where P_t and P_r are the numbers of transmit and receive elements, the per-vector equalization in the OSDM system is based on the $M \times M$ channel submatrices $\{\mathbf{H}_n\}$.

2) Receiver Processing: The turbo detection processing in this paper differs from that given in [31] in aiming to iteratively mitigate IVI other than ICI. On the other hand, regarding ISI suppression, SC-FDE (e.g., [21]) is normally performed blockwise since the channel matrix is circulant and can be diagonalized by the DFT matrix $\mathbf{F}_K$. In contrast, the ISI in OSDM systems is confined within each vector and the circulant structure is no longer held for the channel submatrices $\{\mathbf{H}_n\}$; therefore, extra frequency (un)shifting operations, i.e., post- (pre)multiplication by $\mathbf{\Lambda}_M^n$ ($\mathbf{\Lambda}_M^{nH}$), are needed for equalizing the nth vector [cf., Fig. 3]. Recalling that SCM is also deemed as DFT-precoded OFDM [32], in this perspective, we can consider OSDM as a form of generalized multicarrier modulation precoded with $\{\mathbf{F}_M \mathbf{\Lambda}_M^n\}$.

B. Computational Complexity

We here focus on the algorithms of channel estimation and equalization in the proposed OSDM receiver. For each turbo iteration, the computational complexity in terms of complex multiplications (CMs) are summarized in Table I, where we define $\bar{I} = 2I + 1$, and $\Sigma_{\bar{I}} = (\bar{I}^3 + 3\bar{I}^2 - \bar{I})/3$ denotes the complexity of solving a linear system of $\bar{I}$ equations with the Gaussian elimination method.

1) Channel Estimation: Clearly, compared with the computations of (14) and (15) at $\beta = 0$, the ALS algorithm for joint channel estimation when $\beta > 0$ involves a larger complexity. However, it is interesting to note that the overall complexity is still kept on the same order, i.e., about $\mathcal{O}(M\log_2 M)$ per update, since M is usually much larger than N and I over UWA channels with long delay spreads. This merit is mainly attributed to two characteristics of the designed ALS algorithm. First, the CIR estimation can be implemented by M-point IDFTs, and no matrix inversion is needed [cf., (56)]. Second, a divide-and-conquer strategy is used for the phase estimation, where $\bar{M}\bar{I}$ coefficients are interleaved and partitioned into $\bar{M}$ vectors of length $\bar{I}$ to avoid inverting a large matrix [cf., (62)].

2) Channel Equalization: As mentioned above, we exploit the structure of the channel submatrix in (24), the inverse of which can then be decomposed as (28) accordingly, i.e., two frequency shifts, two DFT operations, and a diagonal matrix inversion. This observation inspires us to perform channel equalization in the frequency domain [cf., (30)], instead of inverting the channel submatrix directly in (27). As a result, compared with the OSDM receiver schemes in [13] and [14], the per-vector computational complexity of channel equalization is significantly reduced from $\mathcal{O}(M^3)$ to $\mathcal{O}(M\log_2 M)$. Moreover, for a multichannel receiver case, we can readily verify from (34) that the complexity of channel equalization is kept linear with the number of receive elements P.

V. NUMERICAL SIMULATIONS

Throughout this section, we consider a coded OSDM system with blocks of length $K = 1024$ and duration $T = 256$ ms. Thus, the symbol sampling period is $T_s = T/K = 0.25$ ms, and the total signal bandwidth is BW $= 1/T_s = 4$ kHz. On each vector, the source bits are appended by a 4-bit CRC and a 2-bit all-zero termination code, i.e., we have $M_t = 6$. The resulting sequence is then encoded using a rate $R_c = 1/2$ convolutional
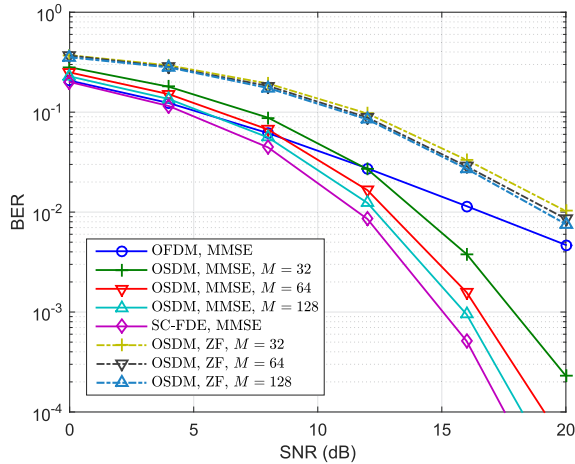
Fig. 4.   BER performance comparison among OFDM, SC-FDE, and OSDM with different vector sizes (over time-invariant channels).

Fig. 5.   BER performance comparison of OSDM systems equipped with different numbers of receive elements (over time-invariant channels).

code with polynomials $(5, 7)$, passed through a random interleaver, and mapped onto a QPSK constellation, i.e., $Q = 2$. Moreover, we insert a CP of length $K_g = 32$ and use a carrier frequency of $f_c = 6$ kHz.

The simulated UWA channel has symbol-spaced paths with maximum memory length $L = 20$, which corresponds to a multipath delay spread of $\tau_{\max} = 5$ ms. Independent Rayleigh fading taps are adopted with an exponentially decaying power delay profile, where the average power difference between the first and last taps is 6 dB. Furthermore, at the receiver, the time-varying phase values $\{\theta_k | k = 0, \ldots, K - 1\}$ during each block are generated by an update equation

$$\theta_{k+1} = \theta_k + 2\pi\epsilon T_s + \xi_k \tag{39}$$

where $\epsilon = a_\Delta f_c$ is the postresampling CFO with a_Δ being the estimation error of the Doppler scaling factor, and ξ_k denotes the extra phase distortion caused by other channel time variation effects. We here model $\{\xi_k\}$ as i.i.d. random variables drawn from a real Gaussian distribution $\mathcal{N}(0, \sigma_\xi^2)$.

Based on the above settings, the performance of the proposed OSDM system is evaluated in three aspects as follows.

A. Frequency-Domain Equalization

We start with evaluating the performance of the per-vector frequency-domain equalization in OSDM systems. To isolate its effect, we temporarily disable the turbo iteration and directly measure the uncoded bit-error rate (BER) at the output of the equalizers (before decoding). Moreover, the channel is assumed to be time-invariant for simplicity.

In Fig. 4, our focus is on the OSDM systems with various vector lengths $M = 32, 64, 128$ and single-element reception. Since the condition $M > L$ is met for all cases, by treating $\mathbf{d}_0$ as the pilot vector, channel estimation in the OSDM systems can be easily performed by using (14). Then, ZF and MMSE equalization follow and their uncoded BERs are plotted. Also, the performances of conventional OFDM and SC-FDE (equivalent to OSDM with $M = 1$ and $M = K$) with MMSE equaliza-
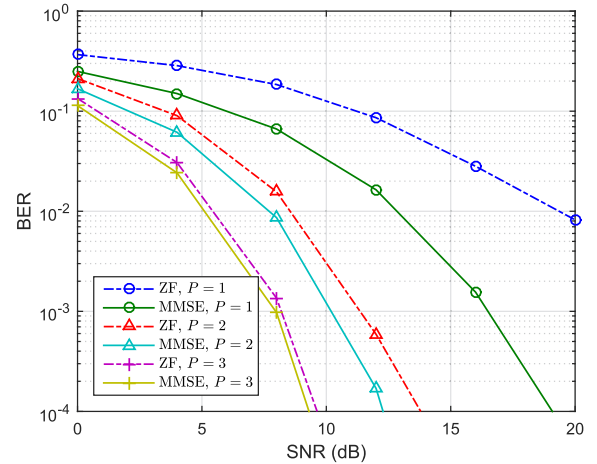
tion based on perfect channel estimates are included to serve as benchmarks. It can be seen that when equipped with MMSE equalizers, the OSDM system outperforms its OFDM counterpart in the high signal-to-noise ratio (SNR) regime, and the performance advantage increases with the vector length M. The reason behind this is that the OSDM system implicitly enjoys an intravector frequency diversity, thanks to being precoded with $\{\mathbf{F}_M \mathbf{\Lambda}_M^n\}$. As expected, in this case, SC-FDE provides a lower bound on the MMSE equalization performance, since it corresponds to the longest vector length. On the other hand, if ZF equalization is used, the BER performance degrades considerably due to its noise enhancement effect caused by the ill-conditioned channel submatrices $\{\mathbf{H}_n\}$, while the performance gain brought by increasing M is now trivial. A detailed theoretical analysis of the diversity order can be found in [18].

The inferior performance of the OSDM system with ZF equalization can be improved by introducing multichannel combining at the receiver. As shown in Fig. 5, for OSDM systems with fixed vector length $M = 64$, when the number of receive elements P increases, both MMSE and ZF equalization produce lower BERs; however, the performance gap between them becomes much narrower.

B. Joint CIR and Phase Estimation

We now continue with time-varying channels and evaluate the performance of joint CIR and phase estimation based on the proposed ALS algorithm. Although, due to the low velocity of acoustic waves (nominally 1500 m/s), the Doppler scaling factor at the receiver front end is typically on the order of 10^{-4} to 10^{-3}, the time variation in the received signal can be expected to reduce greatly after resampling. As such, in the following simulations, we set the residual Doppler scaling factor a_Δ to $[0 : 0.2 : 1] \times 10^{-4}$, and the standard deviation $\sigma_\xi = 2\pi a_\xi f_c T_s$ with $a_\xi = 0.2 \times 10^{-4}$ [cf., (39)].

Consider an OSDM system with vector length $M = 128$. The input SNR of the OSDM system is fixed to 25 dB, while the measured output SNR of MMSE equalization is
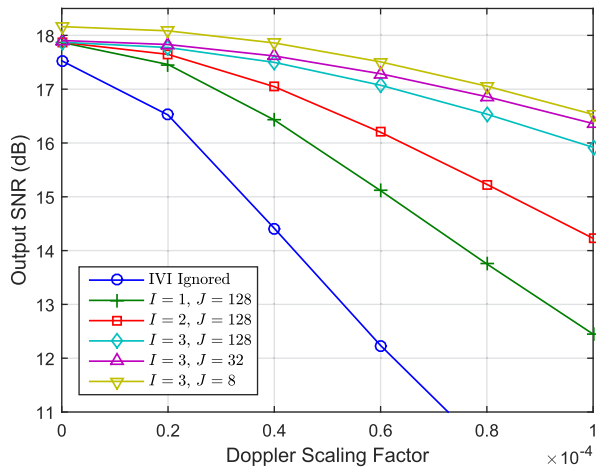
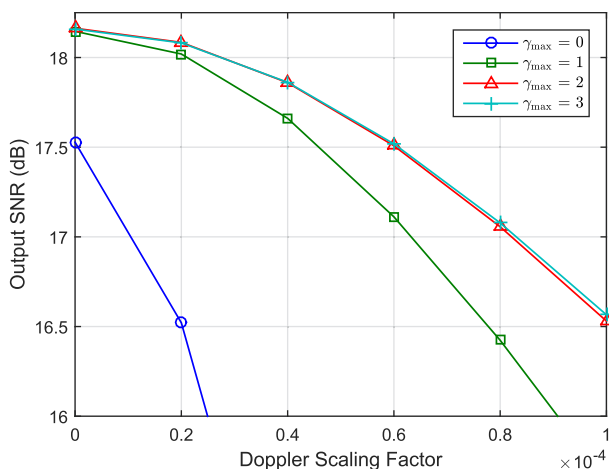Fig. 6. Output SNR performance of the OSDM receiver for different channel modeling parameters I and J.

Fig. 8. BER performance comparison between the OSDM system proposed here and the D-OSDM system in [14].

Fig. 7. Output SNR performance of the OSDM receiver for different ALS iterations $\gamma_{\max}$.
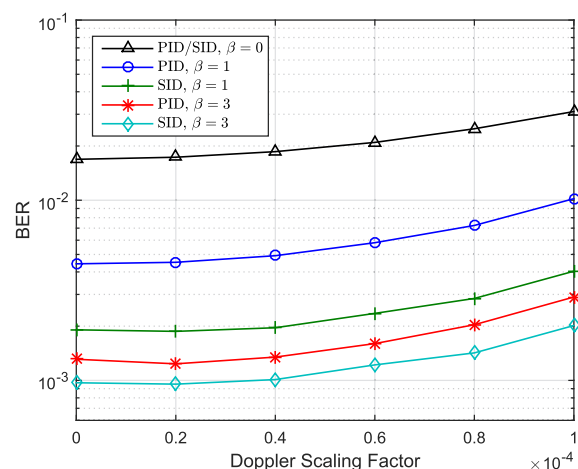
Fig. 9. BER performance comparison between two iterative OSDM detection schemes, i.e., PID and SID.

adopted as the performance metric. Fig. 6 shows the impact of choosing the parameters I and J [cf., (18) and (19)] on the system performance. As a benchmark, if the IVI-ignored processing is applied (which corresponds to the case of $I = 0$ and $J = M = 128$), the output SNR deteriorates rapidly when a_Δ deviates from 0. In contrast, the ALS algorithm has a capability of jointly estimating the channel and time-varying phase. Moreover, by increasing I and/or decreasing J, IVI can be reconstructed and then cancelled with more accuracy. Higher output SNRs are thus achieved at the cost of an increase in computational complexity.

Furthermore, since the ALS algorithm performs joint CIR and phase estimation in an iterative way, its convergence property is shown in Fig. 7, where $\gamma_{\max}$ denotes the number of ALS iterations [cf., Appendix B], and we set $I = 3$ and $J = 8$. It can be observed that while the first two iterations yield a significant improvement on the output SNR of the OSDM system, the performance gain of further iterations becomes negligible. For practical use, only two to three iterations are usually sufficient for convergence of the ALS algorithm.
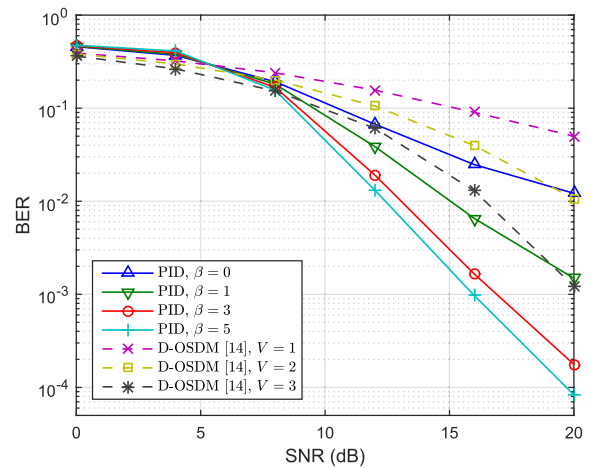
C. Iterative OSDM Detection

In this section, we further take decoding into account and discuss the performance of the iterative OSDM detection. Bandwidth efficiency and BER performance comparisons are first conducted between the OSDM system proposed in this paper and the D-OSDM system in [14]. Here, we set the residual Doppler scaling factor to $a_\Delta = 1 \times 10^{-4}$ and the vector length to $M = 64$. For the D-OSDM system, since $2V$ zero vectors have to be inserted around the pilot vector and each of the U data vector groups, where V is the maximum discrete Doppler shift, its bandwidth efficiency can be computed (with our notation) by

$$\eta_{\text{D-OSDM}} = \frac{QM\left[N - 2V\left(U + 1\right)\right]}{MN + K_{\text{g}}}. \qquad (40)$$

In this simulation, we set $U = 1$ to minimize the overhead of zero vectors, and select $V = 1, 2, 3$, which correspond to the bandwidth efficiencies $\eta_{\text{D-OSDM}} = 1.45, 0.97, 0.48$ b/s/Hz, respectively. On the other hand, the bandwidth efficiency of the

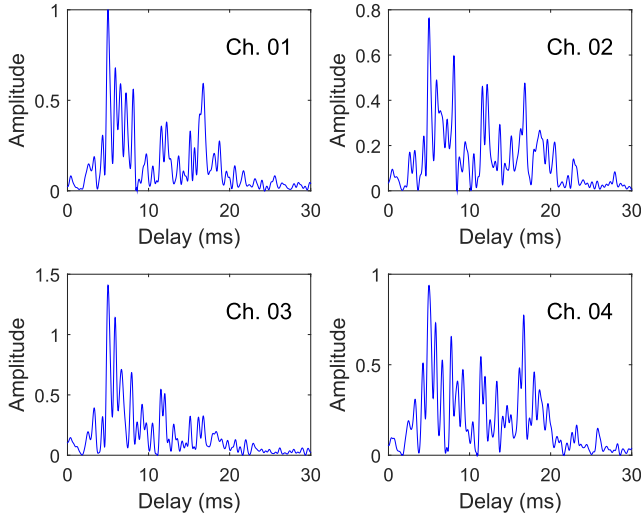Fig. 10.   A snapshot of measured CIRs on each receiver element (Channel 01 through 04).

Fig. 11.   Time-varying CIR on Channel 01 during 30 s.

OSDM system in this paper is

$$\eta = \frac{M_a(N-1)}{MN + K_g}. \tag{41}$$

For the assumed settings, we have $M_a = QMR_c - M_t = 58$ and $\eta = 0.82$ b/s/Hz, which lies between that of the D-OSDM system with $V = 2$ and $V = 3$. Fig. 8 demonstrates the BER performance of the two OSDM systems, where our iterative OSDM detection is embodied by the PID scheme (with ZF equalization for fair comparison). It is interesting to note that in the high-SNR regime, PID has a comparable performance to the D-OSDM system with $V = 2$ even at the initial iteration, i.e., $\beta = 0$. Moreover, when $\beta \geq 3$, it outperforms the D-OSDM system with $V = 3$. This observation indicates that compared to insertion of zero vectors as in the D-OSDM system, it may be favorable to use the frequency band to perform coding, by which a lower BER can be achieved with the aid of iterative detection.

Furthermore, Fig. 9 compares the iterative detection performance of the PID and SID schemes at SNR = 15 dB with various Doppler scaling factors. Since both schemes perform the same preprocessing, their performances are identical at the initial iteration. However, as the iterations progress, SID starts to offer a performance advantage over PID because of its ability to immediately decode and feed back the soft information of the current equalized symbol vector.

VI. EXPERIMENTAL RESULTS

In this section, we present preliminary underwater field test results of the proposed OSDM system. The experiment was conducted at the Danjiangkou reservoir, Henan Province, China, in January 2016. The water depth was varying from 30 to 50 m. Two ships were used as transceiver platforms and deployed 3 km apart. The OSDM signal was transmitted from a depth of about 20 m and received by a four-element vertical array (consisting of Channel 01 through 04) at the same depth with interelement
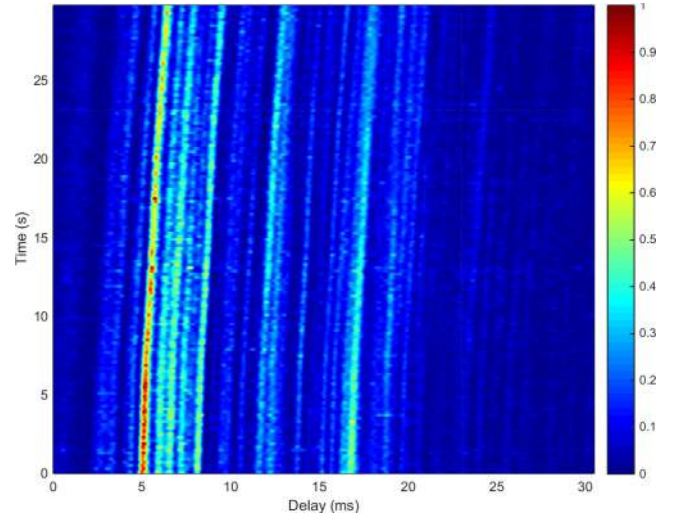
spacing 0.25 m. A typical example of the measured CIRs is shown in Fig. 10, where for comparison purposes, all impulse responses have been commonly normalized by the strongest amplitude in that of Channel 01. It can be seen that the multipath delay spread $\tau_{\max} \approx 30$ ms. Moreover, Fig. 11 displays the time-varying impulse response of Channel 01, which is estimated by performing a train of linear frequency-modulated (LFM) chirp correlations. Since no platform motion was involved, the experimental channels exhibited only slow time variations. Within an observation duration of 30 s, the multipath structure was lagged by 1.49 ms, corresponding to a Doppler scaling factor of -4.97×10^{-5}.

Over these UWA channels, there were a total of 16 data packets transmitted consecutively, each of which has the structure shown in Fig. 12. It comprises four OSDM blocks separated by blank intervals, with two LFM probes inserted for both synchronization and Doppler estimation purposes. The experimental OSDM parameters were nearly the same as those used in Section V. The only difference is that we fixed $M = K_g = 128$ in the experiment to guarantee that: 1) the CP was long enough, i.e., $T_g = K_g T_s \geq \tau_{\max}$; and 2) the assumption $M > \tau_{\max}/T_s = 120$ was valid. The resultant bit rate of the OSDM system can be computed as

$$\frac{M_a(N-1)}{T + T_g} \approx 2.965 \text{ kb/s}. \tag{42}$$

Furthermore, at the receiver, since the Doppler scaling factor is only on the order of 10^{-5}, the front-end resampling is deliberately skipped, and thus the task of compensating for the time variations is left to the iterative OSDM detector. We first set the channel time variation parameters to $I = 2$ and $J = 16$, and use the BER as a performance metric. The BERs of the proposed PID and SID schemes are listed in Tables II and III, respectively, from which similar observations as those in the simulations can be readily made as follows.

1) With SIC improved via the immediate soft information update of the current symbol vector, it is reasonable to say that SID can produce superior performance over PID,
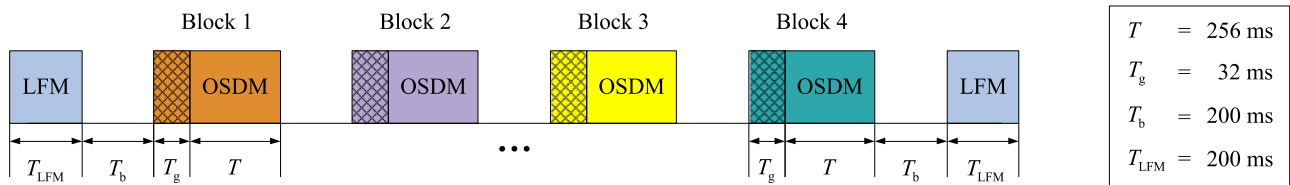
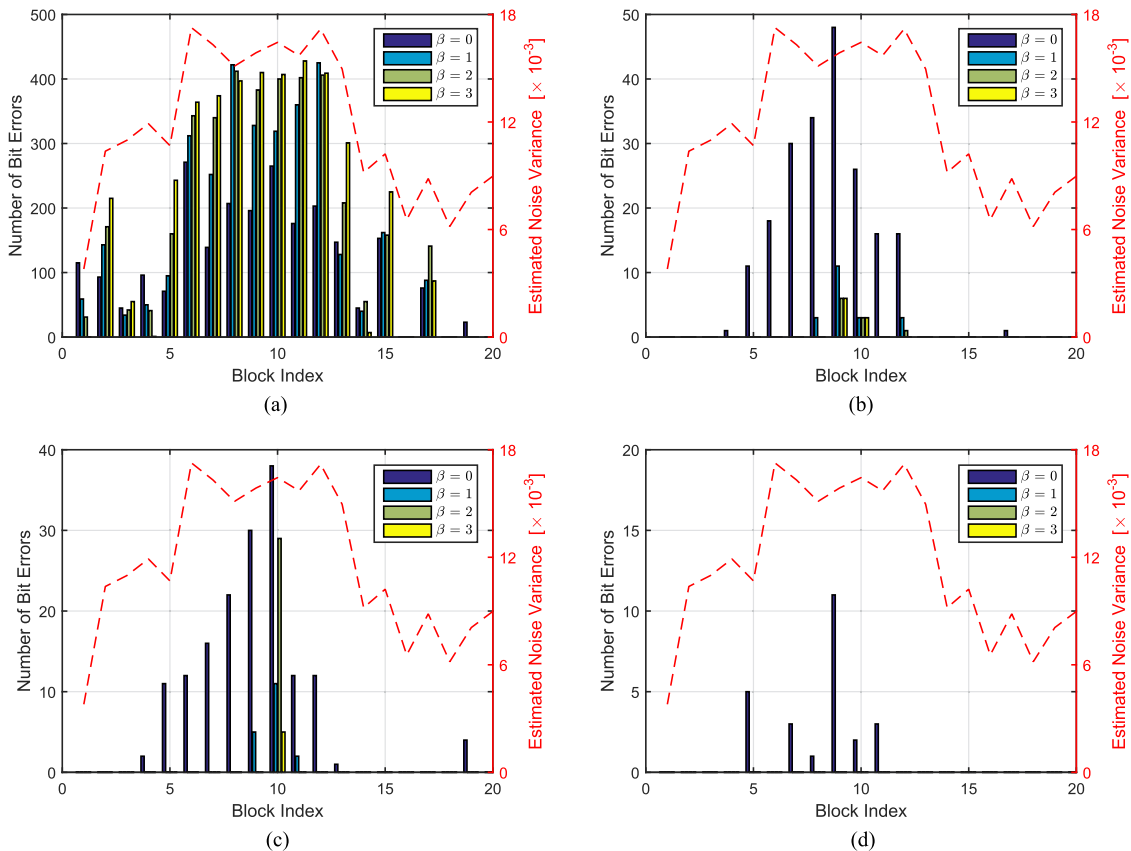Fig. 12. Structure of the transmitted OSDM packet.

Fig. 13. Number of bit errors of the proposed OSDM receiver at each iteration during blocks 1–20. (a) Single-channel ZF equalization. (b) Single-channel MMSE equalization. (c) Two-channel ZF equalization. (d) Four-channel ZF equalization.

TABLE II
BER RESULTS OF THE PID SCHEME

Num. of Channels	Equalization	Iter. No.			
		$\beta = 0$	$\beta = 1$	$\beta = 2$	$\beta = 3$
$P = 1$	ZF	9.14×10^{-2}	11.8×10^{-2}	13.2×10^{-2}	13.6×10^{-2}
	MMSE	3.81×10^{-3}	3.84×10^{-4}	2.01×10^{-4}	1.83×10^{-4}
$P = 2$	ZF	4.50×10^{-3}	7.68×10^{-4}	5.31×10^{-4}	9.15×10^{-5}
	MMSE	7.87×10^{-4}	0	0	0
$P = 4$	ZF	4.57×10^{-4}	0	0	0
	MMSE	1.83×10^{-4}	0	0	0

TABLE III
BER RESULTS OF THE SID SCHEME

Num. of Channels	Equalization	Iter. No.			
		$\beta = 0$	$\beta = 1$	$\beta = 2$	$\beta = 3$
$P = 1$	ZF	9.14×10^{-2}	11.7×10^{-2}	12.6×10^{-2}	13.1×10^{-2}
	MMSE	3.81×10^{-3}	3.66×10^{-4}	9.15×10^{-5}	9.15×10^{-5}
$P = 2$	ZF	4.50×10^{-3}	7.68×10^{-4}	4.03×10^{-4}	5.49×10^{-5}
	MMSE	7.87×10^{-4}	0	0	0
$P = 4$	ZF	4.57×10^{-4}	0	0	0
	MMSE	1.83×10^{-4}	0	0	0

although the BERs of these two schemes are the same in some cases (e.g., when $P = 2$ and $\beta = 1$ with ZF equalization) due to limited experimental data.

2) By utilizing the noise variance estimated in neighboring blank intervals of duration T_b, MMSE equalization outperforms its ZF counterpart. Their performance gap is

impressive especially when single-channel processing is adopted, i.e., $P = 1$.

3) Whatever the choice for the detection scheme (PID or SID) or equalization method (ZF or MMSE), the OSDM system performance improves as the number of channels P or iterations β increases. In particular, it is observed that ZF
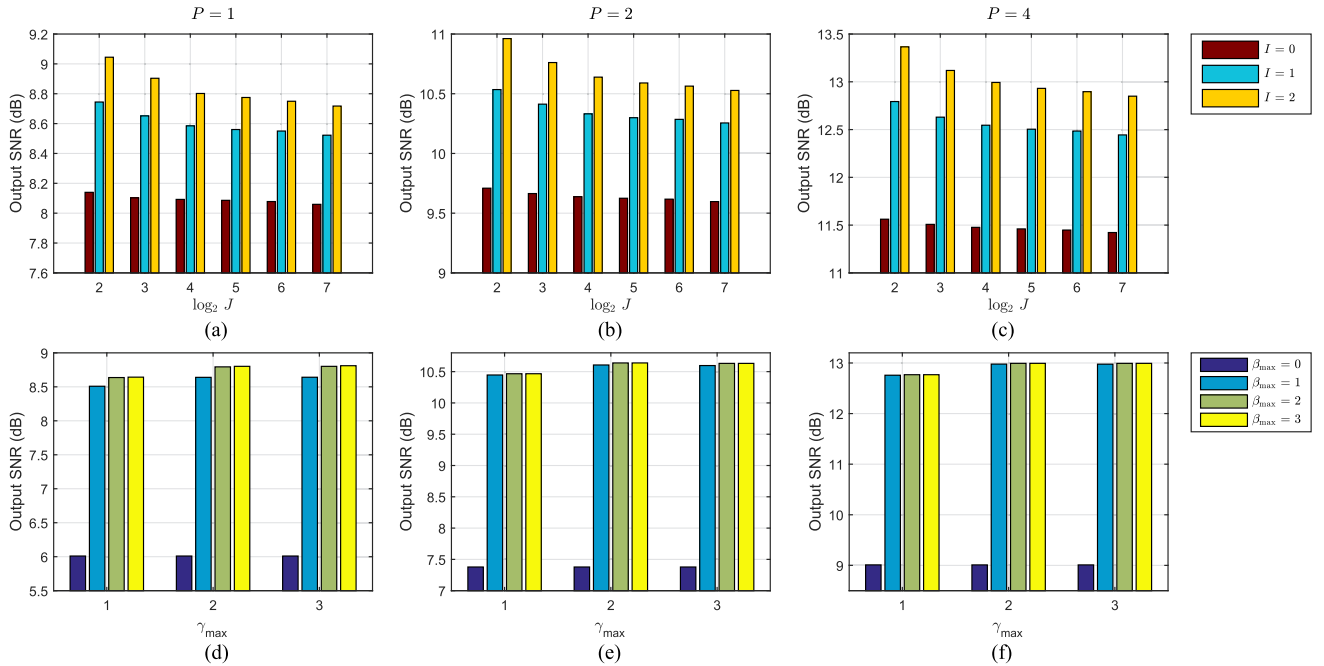
Fig. 14. Output SNRs of the experimental OSDM system for different receiver parameters. (a)–(c) Output SNRs corresponding to various channel modeling parameters I and J with $P = 1, 2$, and 4, respectively. Iteration parameters are here fixed at $\beta_{\max} = 3$ and $\gamma_{\max} = 2$. (d)–(f) Output SNRs corresponding to various iteration parameters $\beta_{\max}$ and $\gamma_{\max}$ with $P = 1, 2$, and 4, respectively. Channel modeling parameters are here fixed at $I = 2$ and $J = 16$.

and MMSE equalization achieve error-free transmissions at iteration $\beta = 1$ with $P = 4$ and 2 channels, respectively.

However, it is noteworthy that both iterative detection schemes fail to converge in the case of single-channel ZF equalization. Let us take a closer look to explain this phenomenon now. In Fig. 13, we consider four receiver settings and plot the number of bit errors at each iteration during OSDM blocks 1–20 (i.e., over the first five packets). Meanwhile, the noise variances estimated for each block are also provided for comparison. It can be seen that there exists a correlation between the system performance and the noise variance. Roughly speaking, the OSDM receiver produces more bit errors over the duration where the noise curve rises up. This observation implies that the performance degradation of single-element ZF equalization is mainly due to the noise enhancement effect. In contrast, by taking into account the noise explicitly or introducing spatial diversity, the performance of the OSDM receiver suffers much less from the SNR reduction with MMSE equalization or multichannel combining.

Furthermore, we inspect the experimental output SNRs corresponding to different choices of the parameters I, J, $\beta_{\max}$, and $\gamma_{\max}$. The OSDM receiver here adopts the PID scheme and MMSE equalization with $P = 1, 2, 4$ channels. First, from Figs. 14(a)–(c), it can be seen that, as expected, the output SNR improves when the Doppler span parameter I increases or the quasi-static subvector size J decreases. However, compared with the substantial performance gains achieved by expanding I, the output SNR shows a weak dependence on J. This is reasonable because the Doppler effects in the experimental channels were not severe, and thus only slow variations appear along the diagonals of the phase submatrices $\{\mathbf{G}_i\}$. As an extreme example, when $I = 0$, the benefit of shortening J becomes negligible,

since in this case the system performance is limited mainly by IVI rather than intravector time variations. Second, as for the iteration parameters $\beta_{\max}$ and $\gamma_{\max}$, Figs. 14(d)–(f) demonstrate that the output SNR saturates quickly as $\beta_{\max}$ increases, while it stays almost constant when $\gamma_{\max} \geq 1$. This suggests that for moderate channel Doppler scales, the proposed OSDM receiver needs only a few iterations to guarantee convergence, which may offer some savings in complexity.

VII. Conclusion

OSDM is a generalized modulation scheme connecting OFDM and SC-FDE. Analogous to ICI induced in OFDM systems, OSDM suffers from IVI over time-varying channels. In this paper, an OSDM system is proposed for UWA communications. It does not need insertion of zero vectors, and performs encoding vectorwise at the transmitter. Accordingly, two iterative detection schemes, PID and SID, are also provided at the receiver, where to counteract the effects of the UWA channel, an ALS algorithm is presented for time-varying channel estimation and a per-vector channel equalizer is designed for IVI and ISI cancellation.

The proposed OSDM system achieves: 1) significant complexity reduction on channel equalization by performing per-vector equalization in the frequency domain; and 2) better BER performance by utilizing bandwidth resources for encoding instead of inserting zero vectors, and with the aid of iterative detection. The results of numerical simulations and a field experiment suggest that OSDM is a promising candidate for high-rate communications over time-varying UWA channels, offering more flexible configurations than the conventional OFDM and SC-FDE.

APPENDIX A
PROOF OF (7)–(10)

Since $\tilde{\mathbf{H}}$ in (5) is a $K \times K$ circulant matrix, it can be diagonalized by the DFT matrix, i.e.,

$$\tilde{\mathbf{H}} = \mathbf{F}_K^H \text{diag}\{[H_0, H_1, \ldots, H_{K-1}]\} \mathbf{F}_K$$
$$= \mathbf{F}_K^H \mathbf{P}_{N,M} \bar{\mathbf{H}} \mathbf{P}_{N,M}^H \mathbf{F}_K \qquad (43)$$

where

$$\bar{\mathbf{H}} = \begin{bmatrix} \bar{\mathbf{H}}_0 & & & \\ & \bar{\mathbf{H}}_1 & & \\ & & \ddots & \\ & & & \bar{\mathbf{H}}_{N-1} \end{bmatrix}. \qquad (44)$$

Also, we can factorize $\mathbf{F}_K$ as

$$\mathbf{F}_K = \mathbf{P}_{N,M} (\mathbf{I}_N \otimes \mathbf{F}_M) \mathbf{\Lambda} (\mathbf{F}_N \otimes \mathbf{I}_M) \qquad (45)$$

where

$$\mathbf{\Lambda} = \begin{bmatrix} \mathbf{\Lambda}_M^0 & & & \\ & \mathbf{\Lambda}_M^1 & & \\ & & \ddots & \\ & & & \mathbf{\Lambda}_M^{N-1} \end{bmatrix}. \qquad (46)$$

Then, substituting (43) and (45) into the first equation of (7), we have

$$\mathbf{H} = \mathbf{\Xi}^H \bar{\mathbf{H}} \mathbf{\Xi} \qquad (47)$$

with

$$\mathbf{\Xi} = \mathbf{P}_{N,M}^H \mathbf{F}_K (\mathbf{F}_N^H \otimes \mathbf{I}_M)$$
$$= (\mathbf{I}_N \otimes \mathbf{F}_M) \mathbf{\Lambda} \qquad (48)$$

where, in the derivation of (48), we have used the fact that $\mathbf{P}_{N,M}$ is unitary, i.e., $\mathbf{P}_{N,M}^H \mathbf{P}_{N,M} = \mathbf{I}_K$, and the identity of Kronecker products, i.e., $(\mathbf{A} \otimes \mathbf{B})(\mathbf{C} \otimes \mathbf{D}) = (\mathbf{AC}) \otimes (\mathbf{BD})$, applied to matrices with matching dimensions. Based on (47) and (48), we readily obtain (7) and (8).

As for the phase matrix, let us define an $N \times M$ matrix $\mathbf{\Theta} = [\boldsymbol{\theta}_0, \boldsymbol{\theta}_1, \ldots, \boldsymbol{\theta}_{M-1}]$ with entries $[\mathbf{\Theta}]_{n,m} = e^{j\theta_{nM+m}}$, and an $N \times N$ matrices $\mathbf{\Theta}_m = \text{diag}\{\boldsymbol{\theta}_m\}$, $m = 0, \ldots, M-1$. We can now have

$$\mathbf{P}_{N,M} \tilde{\mathbf{\Theta}} \mathbf{P}_{N,M}^H = \begin{bmatrix} \mathbf{\Theta}_0 & & & \\ & \mathbf{\Theta}_1 & & \\ & & \ddots & \\ & & & \mathbf{\Theta}_{M-1} \end{bmatrix}. \qquad (49)$$

Moreover, it is easy to know that

$$\mathbf{F}_N \otimes \mathbf{I}_M = \mathbf{P}_{N,M}^H (\mathbf{I}_M \otimes \mathbf{F}_N) \mathbf{P}_{N,M}. \qquad (50)$$

Therefore, the matrix $\mathbf{G}$ in (9) can be rewritten as

$$\mathbf{G} = \mathbf{P}_{N,M}^H (\mathbf{I}_M \otimes \mathbf{F}_N) \mathbf{P}_{N,M} \tilde{\mathbf{\Theta}} \mathbf{P}_{N,M}^H (\mathbf{I}_M \otimes \mathbf{F}_N^H) \mathbf{P}_{N,M}$$

$$= \mathbf{P}_{N,M}^H \begin{bmatrix} \tilde{\boldsymbol{\mathcal{G}}}_0 & & & \\ & \tilde{\boldsymbol{\mathcal{G}}}_1 & & \\ & & \ddots & \\ & & & \tilde{\boldsymbol{\mathcal{G}}}_{M-1} \end{bmatrix} \mathbf{P}_{N,M} \qquad (51)$$

where $\tilde{\boldsymbol{\mathcal{G}}}_m = \mathbf{F}_N \mathbf{\Theta}_m \mathbf{F}_N^H$ for $m = 0, \ldots, M-1$. Since $\mathbf{\Theta}_m$ is a diagonal matrix, $\tilde{\boldsymbol{\mathcal{G}}}_m$ is a circulant matrix with first column

$$\frac{1}{\sqrt{N}} \mathbf{F}_N \boldsymbol{\theta}_m = [g_{0,m}, \ldots, g_{N-1,m}]^T. \qquad (52)$$

Substituting matrices $\tilde{\boldsymbol{\mathcal{G}}}_m$ into (51), we arrive at (9) and (10).

APPENDIX B
ALS ALGORITHM FOR JOINT CIR AND PHASE ESTIMATION

To differentiate from the turbo iteration index β in Fig. 2, the iteration index in the ALS algorithm is here denoted by γ. With this notation, supposing the estimates of the CIR $\hat{\mathbf{h}}^{\langle\gamma\rangle}$ and the phase coefficients $\{\hat{\mathbf{g}}_i^{\langle\gamma\rangle}\}$ have been obtained at the γth iteration, we can then compute the channel submatrices $\{\hat{\mathbf{H}}_n^{\langle\gamma\rangle}\}$, the phase submatrices $\{\hat{\mathbf{G}}_i^{\langle\gamma\rangle}\}$, and the Doppler-compensated signal vectors $\{\mathbf{x}_n^{\langle\gamma\rangle}\}$ based on (24), (25), and (26) similarly.

The ALS algorithm is developed in an iterative framework via two-step LS estimation. Similar methods are also adopted for phase noise estimation in OFDM systems (see, e.g., [33]). We here extend it to the proposed OSDM system. Specifically, the first LS step fixes the phase coefficients and updates the CIR estimate. According to (26), it can be derived that

$$\mathbf{x}_n^{\langle\gamma\rangle} = \mathbf{H}_n \mathbf{d}_n + \mathbf{z}_n^{\langle\gamma\rangle}$$
$$= \mathbf{\Lambda}_M^{nH} \mathbf{F}_M^H \mathbf{D}_n (\mathbf{\Gamma}_n \mathbf{h}) + \mathbf{z}_n^{\langle\gamma\rangle} \qquad (53)$$

where $\mathbf{z}_n^{\langle\gamma\rangle}$ is the noise term. Then, premultiplying both sides of (53) by $\mathbf{A}_n = \mathbf{D}_n^{-1} \mathbf{F}_M \mathbf{\Lambda}_M^n$, we arrive at

$$\mathbf{y}_n^{\langle\gamma\rangle} = \mathbf{\Gamma}_n \mathbf{h} + \mathbf{v}_n^{\langle\gamma\rangle} \qquad (54)$$

where $\mathbf{y}_n^{\langle\gamma\rangle} = \mathbf{A}_n \mathbf{x}_n^{\langle\gamma\rangle}$ and $\mathbf{v}_n^{\langle\gamma\rangle} = \mathbf{A}_n \mathbf{z}_n^{\langle\gamma\rangle}$. Furthermore, by stacking all N signal vectors in (54), and defining $\mathbf{\Gamma} = [\mathbf{\Gamma}_0^T, \mathbf{\Gamma}_1^T, \ldots, \mathbf{\Gamma}_{N-1}^T]^T$, $\mathbf{y}^{\langle\gamma\rangle} = [\mathbf{y}_0^{\langle\gamma\rangle T}, \mathbf{y}_1^{\langle\gamma\rangle T}, \ldots, \mathbf{y}_{N-1}^{\langle\gamma\rangle T}]^T$, and $\mathbf{v}^{\langle\gamma\rangle} = [\mathbf{v}_0^{\langle\gamma\rangle T}, \mathbf{v}_1^{\langle\gamma\rangle T}, \ldots, \mathbf{v}_{N-1}^{\langle\gamma\rangle T}]^T$, it follows that

$$\mathbf{y}^{\langle\gamma\rangle} = \mathbf{\Gamma} \mathbf{h} + \mathbf{v}^{\langle\gamma\rangle}. \qquad (55)$$

Since the columns of $\{\mathbf{\Gamma}_n\}$ are mutually orthogonal, i.e., $\mathbf{\Gamma}_n^H \mathbf{\Gamma}_n = M\mathbf{I}_{L+1}$ for any n, the LS estimate of $\mathbf{h}$ at the $(\gamma+1)$th iteration has the form

$$\hat{\mathbf{h}}^{\langle\gamma+1\rangle} = (\mathbf{\Gamma}^H \mathbf{\Gamma})^{-1} \mathbf{\Gamma}^H \mathbf{y}^{\langle\gamma\rangle}$$

$$= \frac{1}{K} \sum_{n=0}^{N-1} \mathbf{\Gamma}_n^H \mathbf{y}_n^{\langle\gamma\rangle}. \qquad (56)$$

Notice that the matrix inversion is avoided in (56) and the estimate $\hat{\mathbf{h}}^{\langle\gamma+1\rangle}$ can be efficiently computed via M-point IDFTs.

Also, from (56), we can obtain the corresponding channel sub-matrices $\{\hat{\mathbf{H}}_n^{\langle\gamma+1\rangle}\}$.

The above channel estimate is then used to construct the second LS problem and further update the phase coefficients. We now substitute $\{\hat{\mathbf{H}}_n^{\langle\gamma+1\rangle}\}$ into (20), which gives

$$\mathbf{x}_n = \sum_{i=-I}^{I} \mathbf{G}_i \hat{\mathbf{H}}_{n-i}^{\langle\gamma+1\rangle} \mathbf{d}_{n-i} + \mathbf{z}_n. \qquad (57)$$

By extracting the $\bar{m}$th subvector, i.e., premultiplying both sides of (57) by $\mathbf{E}_{\bar{m}} = [\mathbf{I}_M]_{\bar{m}J:\bar{m}J+J-1}$, we have

$$\bar{\mathbf{x}}_{n,\bar{m}} = \sum_{i=-I}^{I} g_{i,\bar{m}} \mathbf{E}_{\bar{m}} \hat{\mathbf{H}}_{n-i}^{\langle\gamma+1\rangle} \mathbf{d}_{n-i} + \bar{\mathbf{z}}_{n,\bar{m}}$$

$$= \mathbf{B}_{n,\bar{m}}^{\langle\gamma+1\rangle} \bar{\mathbf{g}}_{\bar{m}} + \bar{\mathbf{z}}_{n,\bar{m}} \qquad (58)$$

where $\bar{\mathbf{x}}_{n,\bar{m}} = \mathbf{E}_{\bar{m}} \mathbf{x}_n$, $\bar{\mathbf{z}}_{n,\bar{m}} = \mathbf{E}_{\bar{m}} \mathbf{z}_n$, and

$$\bar{\mathbf{g}}_{\bar{m}} = [g_{-I,\bar{m}}, \ldots, g_{0,\bar{m}}, \ldots, g_{I,\bar{m}}]^T \qquad (59)$$

$$\mathbf{B}_{n,\bar{m}}^{\langle\gamma+1\rangle} = \mathbf{E}_{\bar{m}} \left[\hat{\mathbf{H}}_{n+I}^{\langle\gamma+1\rangle} \mathbf{d}_{n+I}, \ldots, \hat{\mathbf{H}}_{n-I}^{\langle\gamma+1\rangle} \mathbf{d}_{n-I} \right] \qquad (60)$$

for $\bar{m} = 0, \ldots, \bar{M}-1$. Likewise, by stacking all the $\bar{m}$th subvectors together from $\{\mathbf{x}_n\}$, and defining $\bar{\mathbf{x}}_{\bar{m}} = [\bar{\mathbf{x}}_{0,\bar{m}}^T, \bar{\mathbf{x}}_{1,\bar{m}}^T, \ldots, \bar{\mathbf{x}}_{N-1,\bar{m}}^T]^T$, $\bar{\mathbf{z}}_{\bar{m}} = [\bar{\mathbf{z}}_{0,\bar{m}}^T, \bar{\mathbf{z}}_{1,\bar{m}}^T, \ldots, \bar{\mathbf{z}}_{N-1,\bar{m}}^T]^T$, and $\mathbf{B}_{\bar{m}}^{\langle\gamma+1\rangle} = [\mathbf{B}_{0,\bar{m}}^{\langle\gamma+1\rangle T}, \mathbf{B}_{1,\bar{m}}^{\langle\gamma+1\rangle T}, \ldots, \mathbf{B}_{N-1,\bar{m}}^{\langle\gamma+1\rangle T}]^T$, it yields

$$\bar{\mathbf{x}}_{\bar{m}} = \mathbf{B}_{\bar{m}}^{\langle\gamma+1\rangle} \bar{\mathbf{g}}_{\bar{m}} + \bar{\mathbf{z}}_{\bar{m}}. \qquad (61)$$

Therefore, the LS estimate of $\bar{\mathbf{g}}_{\bar{m}}$ at the iteration $\gamma+1$ is

$$\hat{\bar{\mathbf{g}}}_{\bar{m}}^{\langle\gamma+1\rangle} = \left(\mathbf{B}_{\bar{m}}^{\langle\gamma+1\rangle H} \mathbf{B}_{\bar{m}}^{\langle\gamma+1\rangle} \right)^{-1} \mathbf{B}_{\bar{m}}^{\langle\gamma+1\rangle H} \bar{\mathbf{x}}_{\bar{m}}. \qquad (62)$$

Notice that the computation of (62) only involves inversion of a small matrix with size $(2I+1) \times (2I+1)$. Furthermore, the estimate of the phase coefficients $\{\hat{\mathbf{g}}_i^{\langle\gamma+1\rangle}\}$ can be readily obtained by interleaving, i.e.,

$$\hat{\mathbf{g}}^{\langle\gamma+1\rangle} = \mathbf{P}_{\bar{M},2I+1} \hat{\bar{\mathbf{g}}}^{\langle\gamma+1\rangle} \qquad (63)$$

where $\hat{\mathbf{g}}^{\langle\gamma+1\rangle} = [\hat{\mathbf{g}}_{-I}^{\langle\gamma+1\rangle T}, \ldots, \hat{\mathbf{g}}_0^{\langle\gamma+1\rangle T}, \ldots, \hat{\mathbf{g}}_I^{\langle\gamma+1\rangle T}]^T$ and $\hat{\bar{\mathbf{g}}}^{\langle\gamma+1\rangle} = [\hat{\bar{\mathbf{g}}}_0^{\langle\gamma+1\rangle T}, \hat{\bar{\mathbf{g}}}_1^{\langle\gamma+1\rangle T}, \ldots, \hat{\bar{\mathbf{g}}}_{\bar{M}-1}^{\langle\gamma+1\rangle T}]^T$.

The ALS algorithm terminates when γ reaches a given number $\gamma_{\max}$, or there is no significant decline in the objective function in (21) as the number of iterations increases. If this condition is satisfied at the γ_eth iteration, the ALS algorithm outputs its final estimates at the turbo iteration β as $\hat{\mathbf{h}}^{(\beta)} = \hat{\mathbf{h}}^{\langle\gamma_e\rangle}$ and $\hat{\mathbf{g}}_i^{(\beta)} = \hat{\mathbf{g}}_i^{\langle\gamma_e\rangle}$, for $i = -I, \ldots, I$.

ACKNOWLEDGMENT

REFERENCES

[1] M. Stojanovic and J. Preisig, "Underwater acoustic communication channels: Propagation models and statistical characterization," *IEEE Commun. Mag.*, vol. 47, no. 1, pp. 84–89, Jan. 2009.

[2] M. Stojanovic, J. Catipovic, and J. Proakis, "Phase-coherent digital communications for underwater acoustic channels," *IEEE J. Ocean. Eng.*, vol. 19, no. 1, pp. 100–111, Jan. 1994.

[3] M. Stojanovic, J. A. Catipovic, and J. G. Proakis, "Reduced-complexity spatial and temporal processing of underwater acoustic communication signals," *J. Acoust. Soc. Amer.,* vol. 98, no. 2, pp. 961–972, Aug. 1995.

[4] M. Stojanovic and L. Freitag, "Multichannel detection for wideband underwater acoustic CDMA communications," *IEEE J. Ocean. Eng.*, vol. 31, no. 3, pp. 685–695, Jul. 2006.

[5] S. Roy, T. M. Duman, V. McDonald, and J. G. Proakis, "High-rate communication for underwater acoustic channels using multiple transmitters and space-time coding: Receiver structures and experimental results," *IEEE J. Ocean. Eng.*, vol. 32, no. 3, pp. 663–688, Jul. 2007.

[6] L. Liu, S. Zhou, and J.-H. Cui, "Prospects and problems of wireless communication for underwater sensor networks," vol. 8, no. 8, pp. 977–994, Aug. 2008.

[7] S. Zhou and Z. Wang, *OFDM for Underwater Acoustic Communications*. Hoboken, NJ, USA: Wiley, Jun. 2014.

[8] Y. R. Zheng, J. Wu, and C. Xiao, "Turbo equalization for single-carrier underwater acoustic communications," *IEEE Commun. Mag.*, vol. 53, no. 11, pp. 79–87, Nov. 2015.

[9] D. Falconer, S. Ariyavisitakul, A. Benyamin-Seeyar, and B. Eidson, "Frequency domain equalization for single-carrier broadband wireless systems," *IEEE Commun. Mag.*, vol. 40, no. 4, pp. 58–66, Apr. 2002.

[10] F. Pancaldi, G. Vitetta, R. Kalbasi, N. Al-Dhahir, M. Uysal, and H. Mheidat, "Single-carrier frequency domain equalization," *IEEE Commun. Mag.*, vol. 25, no. 5, pp. 37–56, Sep. 2008.

[11] N. Suehiro, C. Han, T. Imoto, and N. Kuroyanagi, "An information transmission method using Kronecker product," in *Proc. IASTED Int. Conf. Commun. Syst. Netw.*, Sep. 2002, pp. 206–209.

[12] N. Suehiro, C. Han, and T. Imoto, "Very efficient wireless frequency usage based on pseudo-coherent addition of multipath signals using Kronecker product with rows of DFT matrix," in *Proc. Int. Symp. Inf. Theory*, Jun. 2003, pp. 385–385.

[13] T. Ebihara and K. Mizutani, "Underwater acoustic communication with an orthogonal signal division multiplexing scheme in doubly spread channels," *IEEE J. Ocean. Eng.*, vol. 39, no. 1, pp. 47–58, Jan. 2014.

[14] T. Ebihara and G. Leus, "Doppler-resilient orthogonal signal-division multiplexing for underwater acoustic communication," *IEEE J. Ocean. Eng.*, vol. 41, no. 2, pp. 408–427, Apr. 2016.

[15] X.-G. Xia, "Precoded and vector OFDM robust to channel spectral nulls and with reduced cyclic prefix length in single transmit antenna systems," *IEEE Trans. Commun.*, vol. 49, no. 8, pp. 1363–1374, Aug. 2001.

[16] C. Han, T. Hashimoto, and N. Suehiro, "Constellation-rotated vector OFDM and its performance analysis over rayleigh fading channels," *IEEE Trans. Commun.*, vol. 58, no. 3, pp. 828–838, Mar. 2010.

[17] P. Cheng, M. Tao, Y. Xiao, and W. Zhang, "V-OFDM: On performance limits over multi-path rayleigh fading channels," *IEEE Trans. Commun.*, vol. 59, no. 7, pp. 1878–1892, Jul. 2011.

[18] Y. Li, I. Ngebani, X.-G. Xia, and A. Host-Madsen, "On performance of vector OFDM with linear receivers," *IEEE Trans. Signal Process.*, vol. 60, no. 10, pp. 5268–5280, Oct. 2012.

[19] Z. Wang, S. Zhou, G. B. Giannakis, C. R. Berger, and J. Huang, "Frequency-domain oversampling for zero-padded OFDM in underwater acoustic communications," *IEEE J. Ocean. Eng.*, vol. 37, no. 1, pp. 14–24, Jan. 2012.

[20] B. Li, S. Zhou, M. Stojanovic, L. Freitag, and P. Willett, "Multicarrier communication over underwater acoustic channels with nonuniform Doppler shifts," *IEEE J. Ocean. Eng.*, vol. 33, no. 2, pp. 198–209, Apr. 2008.

[21] Y. R. Zheng, C. Xiao, T. Yang, and W.-B. Yang, "Frequency-domain channel estimation and equalization for shallow-water acoustic communications," *Physical Commun.*, vol. 3, no. 1, pp. 48–63, Mar. 2010.

[22] I. Ngebani, Y. Li, X.-G. Xia, S. Haider, A. Huang, and M. Zhao, "Analysis and compensation of phase noise in vector OFDM systems," *IEEE Trans. Signal Process.*, vol. 62, no. 23, pp. 6143–6157, Dec. 2014.

[23] M. Stojanovic, J. Catipovic, and J. G. Proakis, "Adaptive multichannel combining and equalization for underwater acoustic communications," *J. Acoust. Soc. Amer.*, vol. 94, no. 3, pp. 1621–1631, Sep. 1993.

[24] D. Kilfoyle and A. Baggeroer, "The state of the art in underwater acoustic telemetry," *IEEE J. Ocean. Eng.*, vol. 25, no. 1, pp. 4–27, Jan. 2000.

[25] M. Tüchler, A. Singer, and R. Koetter, "Minimum mean squared error equalization using a priori information," *IEEE Trans. Signal Process.*, vol. 50, no. 3, pp. 673–683, Mar. 2002.

[26] P. van Walree and G. Leus, "Robust underwater telemetry with adaptive turbo multiband equalization," *IEEE J. Ocean. Eng.*, vol. 34, no. 4, pp. 645–655, Oct. 2009.

[27] J. W. Choi, T. Riedl, K. Kim, A. Singer, and J. Preisig, "Adaptive linear turbo equalization over doubly selective channels," *IEEE J. Ocean. Eng.*, vol. 36, no. 4, pp. 473–489, Oct. 2011.

[28] L. Bahl, J. Cocke, F. Jelinek, and J. Raviv, "Optimal decoding of linear codes for minimizing symbol error rate," *IEEE Trans. Inf. Theory*, vol. 20, no. 2, pp. 284–287, Mar. 1974.

[29] G. Leus and P. van Walree, "Multiband OFDM for covert acoustic communications," *IEEE J. Sel. Areas Commun.*, vol. 26, no. 9, pp. 1662–1673, Dec. 2008.

[30] B. Li, J. Huang, S. Zhou, K. Ball, M. Stojanovic, L. Freitag, and P. Willett, "MIMO-OFDM for high-rate underwater acoustic communications," *IEEE J. Ocean. Eng.*, vol. 34, no. 4, pp. 634–644, Oct. 2009.

[31] J. Huang, S. Zhou, J. Huang, C. Berger, and P. Willett, "Progressive inter-carrier interference equalization for OFDM transmission over time-varying underwater acoustic channels," *IEEE J. Sel. Topics Signal Process.*, vol. 5, no. 8, pp. 1524–1536, Dec. 2011.

[32] N. Benvenuto, R. Dinis, D. Falconer, and S. Tomasin, "Single carrier modulation with nonlinear frequency domain equalization: An idea whose time has come — Again," *Proc. IEEE*, vol. 98, no. 1, pp. 69–96, Jan. 2010.

[33] Q. Zou, A. Tarighat, and A. Sayed, "Compensation of phase noise in OFDM wireless systems," *IEEE Trans. Signal Process.*, vol. 55, no. 11, pp. 5407–5424, Nov. 2007.

Qunfei Zhang (M'03) received the B.Sc. degree in electrical engineering and the M.S. degree in signal and information processing from Northwestern Polytechnical University, Xi'an, China, in 1990 and 1993, respectively, and the Ph.D. degree in signal and information processing from Xidian University, Xi'an, China, in 2003.

He is currently a Professor at the School of Marine Science and Technology, Northwestern Polytechnical University. His research interests include spectral estimation, array signal processing, underwater communications, and networking.

Jing Han (M'10) received the B.Sc. degree in electrical engineering and the M.Sc. and Ph.D. degrees in signal and information processing from Northwestern Polytechnical University, Xi'an, China, in 2000, 2003, and 2008, respectively.

He is currently an Associate Professor at the School of Marine Science and Technology, Northwestern Polytechnical University. From June 2015 to June 2016, he was a Visiting Researcher at the Faculty of Electrical Engineering, Mathematics and Computer Science, Delft University of Technology, Delft, The Netherlands. His research interests include wireless communications, statistical signal processing, and particularly their applications to underwater acoustic systems.

Sundeep Prabhakar Chepuri (M'16) received the M.Sc. degree (*cum laude*) in electrical engineering and the Ph.D. degree (*cum laude*) from the Delft University of Technology, Delft, The Netherlands, in 2011 and 2016, respectively.

He has held positions at Robert Bosch, India, during 2007–2009, and Holst Centre/imec-nl, The Netherlands, during 2010–2011. He is currently with the Circuits and Systems Group at the Faculty of Electrical Engineering, Mathematics and Computer Science, Delft University of Technology. His research interests include mathematical signal processing, statistical inference, sensor networks, and wireless communications.

Dr. Chepuri received the Best Student Paper Award for his publication at the ICASSP 2015 conference in Australia. He is currently an Associate Editor for the *EURASIP Journal on Advances in Signal Processing*.

Geert Leus (M'01–SM'05–F'12) received the M.Sc. and Ph.D. degrees in electrical engineering from the KU Leuven, Leuven, Belgium, in 1996 and 2000, respectively.

He is currently an "Antoni van Leeuwenhoek" Full Professor at the Faculty of Electrical Engineering, Mathematics and Computer Science, Delft University of Technology, Delft, The Netherlands. He is also a Fellow of EURASIP. His research interests are in the broad area of signal processing, with a specific focus on underwater communications, array processing, sensor networks, and graph signal processing.

Dr. Leus received the 2002 IEEE Signal Processing Society Young Author Best Paper Award and the 2005 IEEE Signal Processing Society Best Paper Award. He was a Member-at-Large of the Board of Governors of the IEEE Signal Processing Society, the Chair of the IEEE Signal Processing for Communications and Networking Technical Committee, and the Editor-in-Chief for the *EURASIP Journal on Advances in Signal Processing*. He was also on the Editorial Boards of the IEEE TRANSACTIONS ON SIGNAL PROCESSING, the IEEE TRANSACTIONS ON WIRELESS COMMUNICATIONS, and the IEEE SIGNAL PROCESSING LETTERS. He is currently a Member of the IEEE Sensor Array and Multichannel Technical Committee, an Associate Editor for the *Foundations and Trends in Signal Processing*, and the Editor-in-Chief for the *EURASIP Signal Processing*.